



UNIVERSITÀ DEGLI STUDI DI TRENTO

DEPARTMENT OF PHYSICS

MASTER DEGREE IN PHYSICS

Optical Bistability As Neural Network
Nonlinear Activation Function

Supervisor:
Dr. Paolo Bettotti

Graduant:
Davide Bazzanella

Co-supervisor:
Dr. Enver Sangineto

20th March 2018

Contents

| | |
|--|-----------|
| Preface | 1 |
| 1 Artificial Neural Networks | 5 |
| 1.1 History | 5 |
| 1.2 Basis of Neural Networks | 6 |
| 1.2.1 Comparison with conventional computers | 8 |
| 1.3 Working Principles of ANNs | 8 |
| 1.3.1 Learning Process | 9 |
| 1.3.2 Validation Process | 10 |
| 1.3.3 Testing Process | 10 |
| 1.3.4 Datasets | 11 |
| 1.4 Feedforward NN | 11 |
| 1.4.1 Perceptron | 11 |
| 1.4.2 Other Types of NNs | 13 |
| 1.5 ANN Simulation | 13 |
| 1.5.1 PyTorch | 14 |
| 1.5.2 Dataset | 15 |
| 1.5.3 Simulated ANN operation | 16 |
| 2 Integrated Photonics | 19 |
| 2.1 Silicon Photonics | 19 |
| 2.2 Guided-wave photonics | 21 |
| 2.2.1 Waveguides | 21 |
| 2.2.2 Microring optical cavity | 25 |
| 2.3 Nonlinear Optics | 31 |
| 2.3.1 Electronic nonlinearities | 31 |
| 2.3.2 Charge carrier nonlinearities | 32 |
| 2.3.3 Thermal nonlinearities | 33 |
| 2.3.4 Nonlinear perturbation of microring response | 33 |
| 2.4 Integrated photonics applied to ANNs | 36 |
| 2.4.1 Weighted sum of inputs | 36 |
| 2.4.2 Nonlinear Activation Function | 37 |
| 2.4.3 Simulations | 37 |
| 3 Samples, setup and experiments | 41 |
| 3.1 The samples | 41 |
| 3.1.1 Initial characterization | 42 |
| 3.2 Characterization of the Activation Function | 46 |
| 3.2.1 Bistability wavelength dependence | 47 |
| 3.3 Test of a Trained ANN | 49 |
| 3.3.1 Optical bistability as nonlinear activation function | 49 |

| | |
|--|-----------|
| 3.3.2 Optical bistability vs ReLU and Logistic | 50 |
| Conclusions | 51 |
| Bibliography | 53 |
| Aknowledgements | 57 |

Index

critical angle, 15

effective absorption coefficient, 16

effective refractive index, 16

Free Spectral Range (FSR), 20

Snell's law, 15

Preface

The research field

Research in the field of artificial neural networks has become more and more popular in the last few decades as the computing power available to the average institution increased further. As a matter of fact, in the last two decades the calculation power which once belonged only to bulky, power hungry, and very expensive supercomputers, gradually became possible also for relatively more compact, efficient, and definitely cheaper servers and workstations.

This trend has been dictated by the fact that artificial neural networks are usually simulated on conventional computers, which are on the other hand based on the von Neumann, or Princeton, architecture. Implementations of this general purpose architecture are able to do any logical computation with a series of instructions. However the downside of this suitability to generic computations is that it is often difficult to parallelize single operations and therefore certain tasks are inherently inefficient, both in energy and in time. Moreover another problem is that it requires explicit programming for each singular task.

The formalization of the von Neumann (or Princeton) architecture dates back to 1945 [1] and it is as old as the first attempt in artificial neural networks [2]. Shortly after, research and industry efforts focused only on the development of the Princeton architecture, choosing it de facto as the primary design for computing devices.

In the recent years, help came from acceleration units known as Graphic Processing Units (GPU), which were developed for a completely different objective. These GPUs, which are nowadays being designed specifically to accelerate calculations of artificial neural network simulations, are able to carry out a restricted set of instruction compared to CPUs, but are much more efficient both in power and in time, because of their parallel execution [3], [4].

Today's software implementations

Between the most famous examples of simulated neural network there certainly are the older Watson supercomputer from IBM and the more recent AlphaGo artificial intelligence. Both of them arose to popularity because they defeated us humans to our own games. Specifically the effort of Watson was aimed at prevailing the most strongest human contestants at *Jeopardy!*, an American television game, and succeeded in 2011. Watson was powered by a IBM supercomputer and used 0.22 MW of power. AlphaGO, nevertheless, is a deep neural network that in 2016, through reinforced learning algorithms, defeated Lee Sedol, considered the most formidable master of Go, a complicated board game [5].

Another interesting case is given by SpiNNaker, of the University of Manchester. It is composed by 10^4 neurons connected by more than 10^7 synapses, and is simulated on over 65 thousand 18-core ARM processors connected together. Unlike the other two, its main goals are to simulate several neural mechanisms, such as the operation of visual cortex. The SpiNNaker system is part of the Human Brain Project (HBP), funded by the European Union [5], [6].

Similarly to SpiNNaker, another effort in gaining better understanding of the human brain is *The Blue Brain Project*, which is leaded by École Polytechnique Fédérale de Lausanne in collaboration with over one hundred other international research institutions and it is funded by the European Union. This project is simulated on IBM Blue Gene supercomputers, each

fitted with more than 100 thousand processors and consuming several MW of power [5].

Present objectives and future trends

We can distinguish two principal objectives in this research field. The first one is a technological objective and is that of developing a more powerful computational instrument. The second objective is instead a topic of more fundamental research: to use the tools of artificial neural networks to better understand biological neural networks such as our brain [6], [7].

If the comprehension of the complex mechanism at the base of our brain has always been a very arduous assignment, the tasks that artificial neural network are facing become increasingly difficult while time passes. Whereas in the past years public and private research groups trained themselves with “easier” problems, such as television or board games, today they are concentrating their efforts on more challenging goals. Probably the most clear example of this tendency is given by the research on autonomous driving, where artificial neural networks are used primarily for real-time processing of data from several sensors [8].

A great number of businesses formed in recent years around these problems and many other will probably do the same for similar areas. It is very likely that to achieve their objectives, even more powerful and complex artificial networks will be required. Therefore more processors will be developed and put together to achieve impressive computing power. However, one cannot expect to increase indefinitely the power, without significant improvements in efficiency. Hence alternatives are sought [9].

Overview of current alternatives to simulations

Apart from the vast majority of the research on neural networks, which is being carried out with simulations on powerful processors, a smaller portion of research is focused on building neural network physically. Great efforts are made nowadays by many research institutions and companies to develop original computing architectures that allow artificial neural networks to run physically, instead of being simulated on conventional computers [9].

The reason why considerable improvements can be expected is that the path of designing hardware devices ad hoc for neural network computation has not yet been covered comprehensively. Major performance or efficiency enhancements are coming from the fact that those new architectures are conceived with parallel execution of specific operations in mind. This, however, makes them inevitably less adaptable to changes, unlike software simulations on conventional computers, which can be modified just by changing few lines of code. A good example is given by size of the network, which in simulation is easily altered, even of orders of magnitude, while in hardware implementations it depends strictly by the architecture features and scalability.

Many of these use the electronics framework, mainly because of the many benefits of the mature silicon technology and its CMOS-compatible production chain. Specifically footprint and efficiency of CMOS devices has not yet stopped to grow since its discovery, in the past century. However, a relatively small portion of these works also inquired simpler network fabrication with organic electronic materials, achieving remarkable results [5].

Among the most interesting projects which uses electronics there are TrueNorth of IBM, Neurogrid of Stanford University, and BrainScaleS designed in Heidelberg and Dresden. The former is part of a long-term research project funded by DARPA and has the aim of building an artificial neural network with the capabilities of brains of small mammals, such as cats or mice. In 2014 IBM showed a chip, named TrueNorth, containing 1 million artificial neurons and 256 millions synapses. This network, relying on more than 5 billion transistors organized on an area of 4.3 cm^2 , consumed only 60 mW. The researcher also proved that connecting 48 of this chips together they obtained the equivalent of the brain of a mouse [5].

Similarly, the intention behind Neurogrid chip is to explore numerous hypothesis concerning mammalian brains, specifically about the inner mechanisms of operation of the cerebral cortex. Stanford’s implementation reaches the line of 1 million neurons, while only requiring 5 W of power consumption. Moreover the communication lines between single neurons, the synapses, are provided by FPGAs and banks of SRAM [5].

Finally the BrainScaleS is built by 20 silicon wafers, each containing 200,000 biologically realistic neurons and 50×10^6 plastic synapses. Likewise SpiNNaker is funded by the European Union and it is part of the Human Brain Project. A particularity of this system is that does not execute pre-programmed code, but evolves according to the physical properties of the devices themselves [6].

Neuromorphic photonics

Besides electronics, other kind of physical implementations have been attempted from research teams. Probably the most intriguing example is given by integrated photonics. Photonics Integrated Circuits (PICs) have never been competitive in comparison to electronics in the development of von Neumann like processors, which are based on boolean logic gates. No photonic integrated logic of comparable performance to electronics has been proposed yet. However, by implementing a computing architecture that adheres to the artificial neural network rules integrated photonics might emerge as a successful platform [10]. Even if research in neuromorphic photonics is just in its embryonic state, many progresses have been accomplished lately. The aim of neuromorphic photonics is to match electronics performances by overcoming it in power consumption, computational speed, and intrinsic suitability to parallel computing.

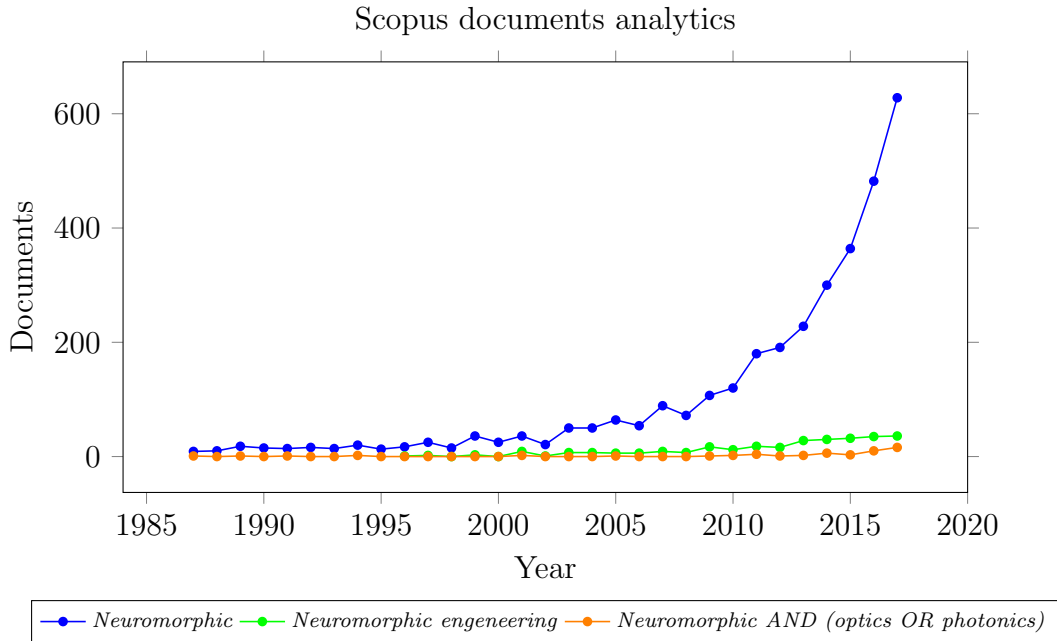


Figure 1: Scopus data on ‘neuromorphic’ vs ‘neuromorphic photonics’

Since PIC manufacturing is not as developed as fabrication of electronic devices, integrated photonics research on artificial neural networks concentrates on integrating single optical devices rather than building a full-grown all-optical network. The great majority of researches integrates optical structures and electronic ones on the same network, building hybrid optoelectronic artificial neural networks. Moreover, the networks implemented mostly are of recursive type or trained with the reservoir computing method. Both of them allow to build functioning ANNs with a low number of (controllable) computing nodes.

My work

My work in this thesis has two related objectives. The primary aim is to implement a proof of concept for a fundamental component of artificial neural networks: the neuron's activation function. I plan to do so by employing the framework made available by integrated photonics. The second intent is to bring together two until now distant fields of research: photonics and machine learning. In fact generating knowledge and tools to be used in common by the two research fields is at least as much important as the primary objective.

The idea at the base of our physical implementation is to employ integrated optical devices, which have been manufactured for other projects, to create a proof of concept for the activation function. Therefore in this work I will study a particular device, a microring resonator, and characterize its response to different inputs, for several working conditions. This device can process information because it has, under certain circumstances, a nonlinear response function to its inputs. Moreover, the same device might be used in another important part of artificial neural network nodes: the weighted sum. With this two parts together one could claim to have built a rudimentary artificial neuromorphic network, the *perceptron* (see Subsection 1.4.1). However, since integrated structures able to carry out a weighted sum of optical signals have already been discussed in literature and it requires less effort to produce acceptable results, it will not be at the center of this study.

During the thesis I achieved two main results. I have demonstrated the use of the nonlinear response of a microring optical cavity to produce an activation function by exploiting the optical bistability regime. In addition, with the aim of testing such response function, I simulated an artificial network with custom activation function by using standard software libraries used by ICT community to model neural networks.

Structure of the thesis

The first chapter of this thesis is intended as an introduction to the world of artificial neural networks. After a brief historical summary, I describe the main aspects of neural networks and their working principles. Then I focus on the description of the simplest type of artificial networks, the feedforward network, and finally an overview on other kind of networks. Later, the chapter is concluded with an introductory description of the Python language and the PyTorch library, used in this work for artificial network simulations.

The second chapter introduces the physics which I will study. Again, after a short explanation on the basic devices used in the field, I will describe in depth the device studied for the task. Having clarified the physics underneath, I ought to explain how I am going to use this physics to implement (part of) an artificial neural network. I will address these topics both from the theoretical point of view and from the numerical one, with simulation of the specific (simplified) system.

The third chapter is dedicated to the description of the experimental work. At the beginning the problem of the selection of the sample is discussed, along with the definition of the device chosen. After, I characterize the different behaviors with detailed data. Finally, an explanation on how the device will be used in the neural network viewpoint and the corresponding tests of operation.

Chapter 1

Artificial Neural Networks

Artificial Neuromorphic Networks (ANNs) are computational systems which elaborate information in a way that is loosely inspired by the operation of biological neural networks (animal brains). Biological networks are superior in performance to computers and extremely more efficient in difficult tasks such as classification (e.g. image recognition) and prediction (e.g. pattern recognition). The underlying idea is to copy some of their mechanisms and exploit them for computational applications. These systems are intrinsically parallel in operation, do not require specific programming to operate, and modify their behavior through a learning process to improve their accuracy in a certain task.

Mathematically speaking, ANNs are a collection of nodes, each one of them elaborates the information and is somehow connected to the other. Artificial networks can be either simulated on computers or physically built on hardware designed ad hoc. At this time, ANNs are mainly implemented by simulations, however the technological progress is withheld by limitation in computing power and efficiency. Training a complex artificial neural network with computers at the state of art might take even weeks. Thus, with the aim of improving performance from simulated networks, research on hardware architectures is surging: digital, analog, electrical, and optical devices are being developed.

1.1 History

It is widely acknowledged that the opening work of this research field was made in 1943 by Warren McCulloch and Walter Pitts, a neurophysiologist and a mathematician respectively. In their research work, they described the operating mechanism of biological neurons by modeling a simple electronic circuit [11].

The following important work was made by Donald O. Hebb, who hypothesized the neural plasticity in 1949 [12]. He pointed out the fact that neural pathways are strengthened each time they are used, a concept known as *Hebbian learning*.

During the late 1950s and the early 1960s, as computers became more powerful, many promising works were published. Some simulated operation of artificial networks on calculators, e.g. Farley and Clark [13] and Rochester [14]. Other produced circuitry that implemented on hardware such networks, e.g. Rosenblatt [2], [15]. However, despite the early successes of neural networks, the traditional computing architecture (von Neumann architecture) was chosen as the preferred computing architecture.

The reason why this happened, probably, was due to several concurring facts. First of all, in the same time period (1969) a research paper by Minksi and Papert [16], which identified two important problems. The basic perceptron was not able to execute the exclusive-or (XOR) operation, unlike the logical circuits at the base of von Neumann architecture. Moreover, the research stated the fact that more complex networks such as multiple- or deep-layered networks

were not possible (at that time) because of the lack of adequate processing power.

In addition to this research, the early successes of some works on neural networks pointed to an overestimation of the artificial neural networks potential, also held back by the technological capacity of the time. Finally, important questions of philosophical nature came to light, such as the fear fueled debate on the impact on our society of a class of computers able to think. This very controversy, i.e. the artificial intelligence (AI) problem, is discussed still today [17].

Sometime during the 1980s the interest for this computing method was reinvigorated. The main stimulation was probably given by a number of works which suggested methods to implement multi-layered networks distributing pattern recognition errors through the all the layers in the network. This method is now called *backpropagation*.

In today's research and technology, artificial neural networks are used in numerous applications. However, the development is made slowly, due to technological limitation in computational power of present processors.

1.2 Basis of Neural Networks

A neural network is a collection of processing elements, or nodes, interconnected in an arbitrary topology. From its input nodes, the network accepts information, which will propagate into the inner nodes through the interconnections and will get elaborated at each node. At the end of the network, there will be a number of output nodes, with the task of reading a portion of the inner nodes. The inner nodes are also called hidden, because they are not meant to be accessible to the external world. A generic scheme of such network is shown in Figure 1.1 on this page.

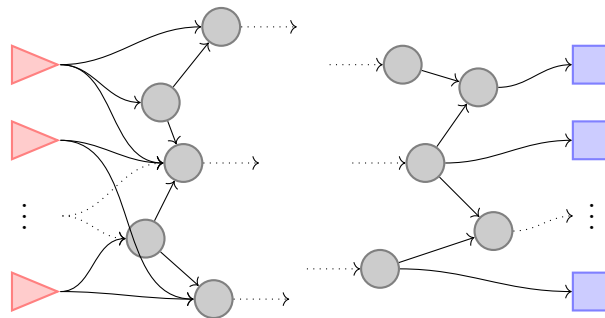


Figure 1.1: Generic scheme of a neural network. Triangles (red) are input nodes, circles (grey) are inner nodes, and squares (blue) are output nodes. Interconnections among nodes are represented by arrows: continuous when both elements are drawn, and dotted otherwise.

Nodes can all implement the same function or behave differently, depending on the type of neural network. The operation of nodes resembles that of animal neurons: various input gets collected and elaborated together to obtain an output, which will become one of the many inputs for subsequent neurons/nodes. Specifically, the most used model for neurons is the McCulloch–Pitts (MCP) neuron. It is divided into two parts, as shown in Figure 1.2: the first part is a weighted sum of the inputs, while the second part is given by the so called activation function.

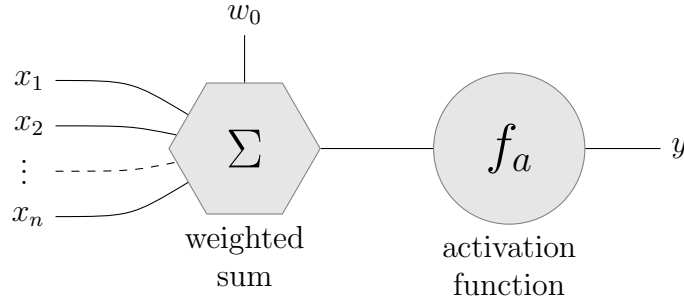


Figure 1.2: Generic node representation. x -values are inputs, y -values are outputs, w_0 is the bias.

The node is described mathematically by equation (1.1)

$$y = f_a \left(w_0 + \sum_{i=1}^n w_i x_i \right), \quad (1.1)$$

where f_a is the activations function, evaluated on the sum of the input x_i weighted with w_i , plus a bias w_0 .

Each node accepts values at its inputs and produces an output accordingly. However, in addition to the input, the output depends also on the node's parameters: the weights and the bias, which are usually changed outside the operative phase of the neural network (see Section 1.3).

Moreover it is mandatory for the activation function $f_a(\cdot)$ to be nonlinear, because otherwise a collection of nodes will result in just a weighted sum of its inputs. Two examples of nonlinear function are shown below in Figure 1.3.

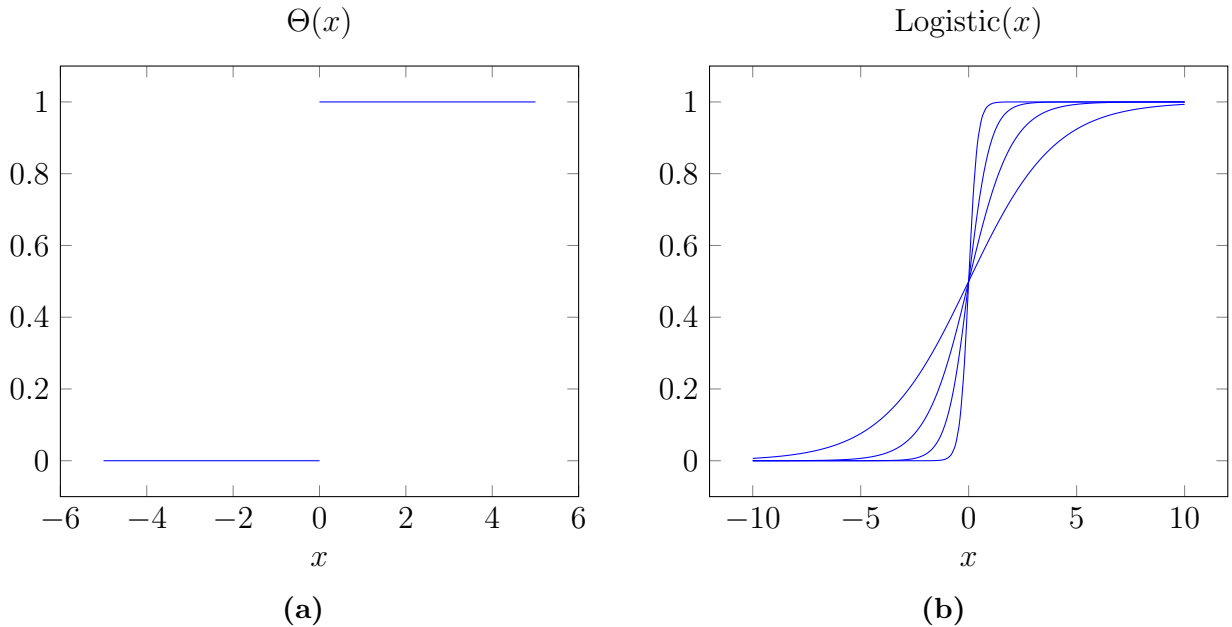


Figure 1.3: Examples of activation function: (1.3a) is the well-known step function, or Heaviside Θ , (1.3b) depicts a few functions from the family of the Logistic functions.

One can distinguish at least three type of nodes in every neural network: input, inner/hidden, and output nodes. Input nodes take one input value, from the outside of the neural network, and pass it on to the inner nodes unchanged. Inner/hidden nodes take many

inputs and generate an output through the activation function. Output nodes, similarly to input nodes, take one input value, from the inside of the NN, and pass it on to the outside.

Standard Representation

The way I depicted a generic neuromorphic network in Figure 1.1 is not the standard representation used in books and research papers. The main difference is that usually weights are commonly represented on the connection between the nodes, which are then designated to apply only the activation function. Moreover the input layer is linear as it feeds the inner nodes with the input data, while the output layer is actually given by the last nonlinear layer of the inner nodes. A generic network is shown in Figure 1.4a.

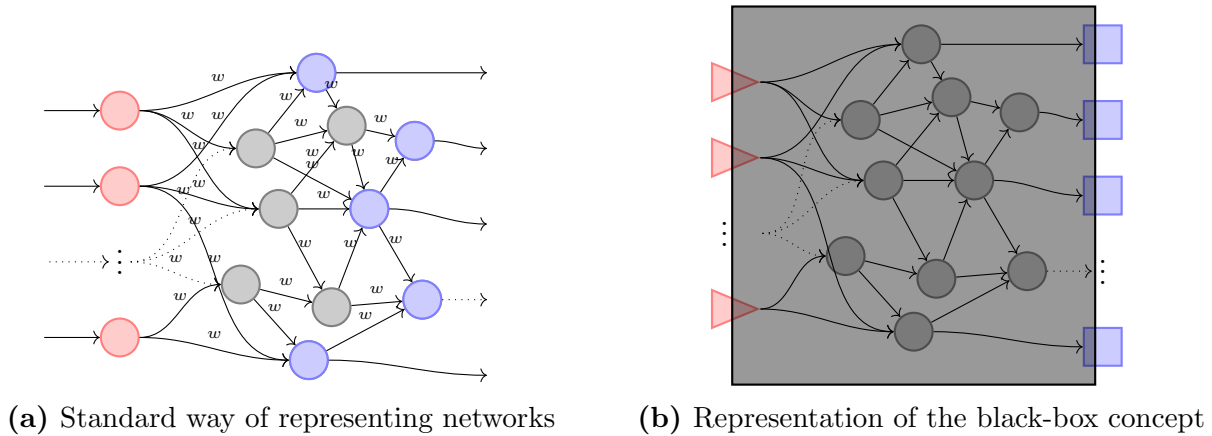


Figure 1.4

On the contrary, I consider the inner nodes as the only place where any kind of elaboration on the data happens. Inner nodes have a number of inputs, which are weighted and summed together to be entered as argument in the activation function. This leads to a natural separation between input/output nodes, which acquire the task of providing data from/to the outside, and inner nodes, which is where the activation function and/or the weighted sum are carried out.

This non-standard description, moreover, is consistent with the idea of functional *black box*, in which input and output are the only visible nodes, while the other are hidden inside, as shown in Figure 1.1.

1.2.1 Comparison with conventional computers

1.3 Working Principles of ANNs

Because of its topology, each neural network will behave in a different manner from other neural networks with diverse, or even similar, arrangements of nodes. Moreover the same neural network will perform a certain task better or worse also depending on how inputs are weighted at each hidden node, and normally those parameters are initialized with a random value at the creation of the network. For this reason, before a neural network is considered ready to perform a task, it usually must go through three training stages: learning phase, validation phase, and testing phase. Every one of these stages is meant to prepare the network to work as required from the designer.

1.3.1 Learning Process

During the learning process the neural network is run on a set of known inputs x , each paired with its correct answer y , or target, in a second set of data. The neural network will produce at the output a third set \hat{y} , which should be as close as possible to the correct answers, when the network works properly. Typically weights among nodes are initialized randomly and the distance of the network outcome from the target function is measured through a loss function. Then weights are modified in order to decrease the loss function to its lowest possible value.

Loss function

The loss function $L(y, \hat{y})$ evaluates the difference between the predicted and the correct answer. Usually, this quantity is linked to the geometrical distance between the predicted output and the target $|\hat{y} - y|$.

The most common loss function is the *mean-square error*. Assuming to have an input set of N examples paired with the same number of targets, and that the outputs and the targets are composed by C values, or classes, the function becomes:

$$L(y, \hat{y}) = f_{MSE}(y, \hat{y}) = \frac{1}{N} \sum_{n=1}^N \sum_{i=1}^C (\hat{y}_{n,i} - y_{n,i})^2, \quad (1.2)$$

where each example in the set is subtracted to its target and then squared. Finally the mean of all squares gives the expected result.

Another commonly used function is the cross-entropy loss (also known as negative log likelihood),

$$L(y, \hat{y}) = f_{CEL}(y, \hat{y}) = -\frac{1}{N} \sum_{n=1}^N \sum_{i=1}^C y_{n,i} \log(\hat{y}_{n,i}), \quad (1.3)$$

which expects positive values at the input. Hence the error $-y \log(\hat{y})$, quantified for each element in each example, is always a positive number. The mean over all examples in the set returns the results.

Alternatively, variations of the previous methods are given by taking the sum of the examples in place of the mean, or by calculating a loss function for each example instead of evaluating it for the whole set.

Weights Update Process

The weights update process is a difficult task, and probably the most computationally expensive one in running a neural network. There is a variety of methods to chose from, depending on the type of artificial network and the resources available.

A widely used algorithm is the gradient descent, from its most simple version to more complex variations such as stochastic gradient descent (SGD). This method updates the weights by subtracting a value proportional to the gradient of the loss function in respect to the weights themselves times a positive factor called *learning rate*, as shown below.

$$w_i|_{n+1} = w_i|_n - lr \cdot \frac{\partial L}{\partial w_i|_n} \quad (1.4)$$

where $w_i|_n$ are the current weights, lr is the learning rate, $\frac{\partial L}{\partial w_i|_n}$ is the first derivative of the loss function in respect to the i -th weight at the current step, and $w_i|_{n+1}$ are the updated weights. This method is equivalent to minimize the error on the loss function, by following the

gradient $\nabla_w L$. This vector lives in the multidimensional space of the loss function $L : \mathbb{R}^W \mapsto \mathbb{R}$, where W is the total number of parameters in the network.

The most efficient ?? algorithm is called *backpropagation*: it computes the first derivative of the loss function L in respect to all the parameters of the network, the weights, starting from the end of the artificial network and going backward toward the input, hence the name backpropagation. Since the number of connections between nodes might be even order of magnitude bigger than the number of nodes, it is simple to understand how large networks are computationally expensive to train.

1.3.2 Validation Process

In the validation process, which happens repeatedly throughout the training process, the neural network is tested of a new set of examples. However, the outcome of this test is not used to change the weights as in the learning phase. Instead, the output is used to prevent overfitting.

Overfitting is the phenomenon in which a neural network is trained over and over on the same set of data. This can train the network to recognize specific features of the samples instead of the more general ones. Therefore, by periodically testing the network on a novel set, i.e. the validation set which is different from the training set, one can reduce or avoid the problem.

Depending on the resources available and the size of the dataset, the validation happens more or less often throughout the learning process.

1.3.3 Testing Process

At the end of the training and validation processes, there is the process of testing the artificial neural network. The network is tested on a new set of data, the test data. This time the predicted outputs are compared to the correct answers, but no weights are changed. Instead, an overall value of the correctness is evaluated and it is often expressed in percentage.

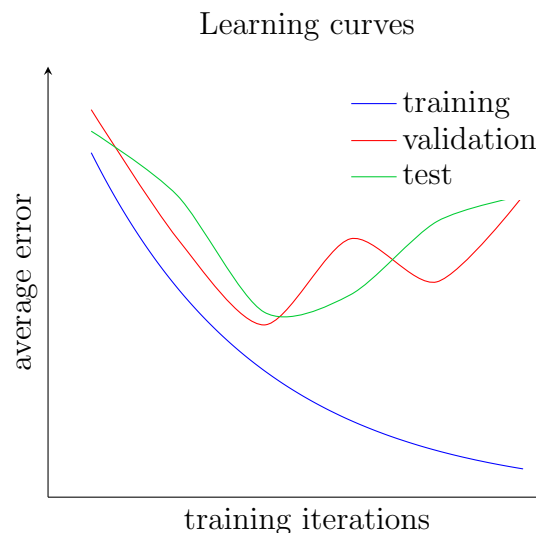


Figure 1.5: The learning curves are the value of the loss function, or criterion, as a function of the training iterations. Both the validation and the test error are usually higher than the error on the training set. Sometimes, to avoid overfitting, the training procedure is stopped at a minimum of the validation learning curve [18].

1.3.4 Datasets

Creating a dataset and splitting it into subsets is another problem to deal with. It is not so simple and straightforward as it appears. For example a dataset which is too big will lead to a longer training time for the network, whereas a too little set will cause a poor training.

The most naive division is in three equal parts, since three are the phases of preparation for any artificial neural network. However, as shown later in Subsection 1.5.2, when the resources dictates otherwise, other subdivision can be implemented. In my case, the decision was to follow the suggestions of the authors of the dataset and divide the examples into a training set and a test set only, with a ratio between the two close to 50%.

1.4 Feedforward NN

The first and most simple type of neural network is called Feedforward. In this kind of neural network, nodes are divided into groups called *layers*. A layer is a collection of nodes that accepts inputs from a preceding group and generate as many outputs as the number of nodes in the layer. Each layer of a Feedforward neural network is connected in series with the others, except for the input layer at the beginning and the output layer at the end. As for the single nodes, the inner layer are called hidden, because usually not accessible.

The information travels from the input to the output and gets elaborated from each hidden layer: there are neither connection between nodes of the same layer, nor loops or feedback between layers. The number of hidden layers and the number of nodes they contain depends on the network topology. Moreover the connection between the layers might be complete, i.e. each node in the layer accepts each input of the preceding layer, in that case the layer is said to be *fully connected*, or sparse as in the case of convolutional layers (see Section 1.4.1).

1.4.1 Perceptron

The most naive topology of a Feedforward neural network is given by the so called *Perceptron*. The Perceptron dates back to the 1957, when the homonym *Perceptron algorithm* was software implemented by Frank Rosenblatt on a computer (IBM 704) and only subsequently in hardware as the *Mark 1 perceptron* [2], [15]. The graph of a generic (single layer) perceptron ANN is shown in Figure 1.6 below.

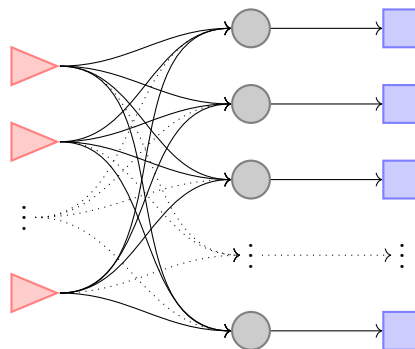


Figure 1.6: Perceptron type neural network: in this representation the perceptron has n inputs and m outputs as well as a hidden layer with m nodes.

By adding more than one hidden perceptron layer to the neural network, one obtain the so called *Multi-Layer Perceptron* (MLP). This allows for more computational complexity ?? When the total number of layer is more than two, the network is called *deep*. A deep MLP is shown in Figure 1.7. In principle any shape is possible, i.e. each layer could have a different

number of nodes, however often the layers at the beginning are wider than the layer at the end of the network ?? Besides the shape, in literature a perceptron is almost always considered fully connected ??

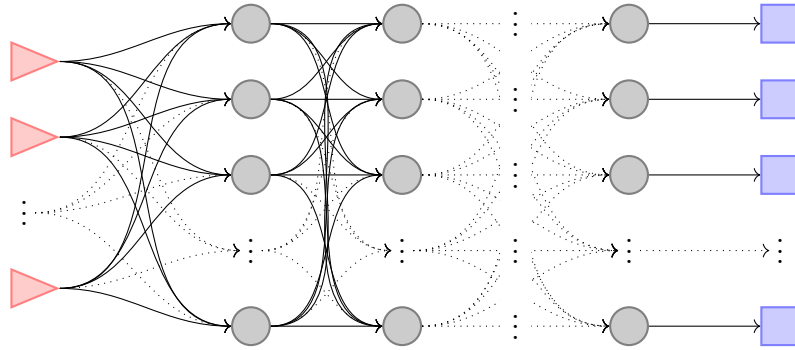


Figure 1.7: Deep Multi-Layer Perceptron (MLP), fully connected.

Other Feedforward NNs

Feedforward neural networks are a large family that includes many other types besides the perceptron one. A few names are autoencoder, time delay, and convolutional neural networks. Autoencoders ANNs are feedforward networks with the same number of input and output nodes, with the purpose of reconstructing its own inputs. For this reason autoencoders employ unsupervised learning. Time delay networks have a feedforward structure and their purpose is to analyze patterns in

Convolutional networks are inspired to the visual cortex, in which neurons are not fully connected their inputs but only to a restricted region. Convolutional neural networks are a type of feedforward network conceived to recognize images without being misled by distortions such as translation, skewing, or scaling. Its input is often represented as a 2D matrix, instead of a 1D vector. This kind of network is usually composed by many layers, the prevalent kind is the convolutional one. This layer performs a two-dimensional convolution over the input matrix of a second 2D matrix of weights, called *feature map*. Thus, each node of the layer operates on a restricted region to understand if a feature is present or not. Commonly the operating regions are overlapping and the feature map is shared among the nodes in the same layer.

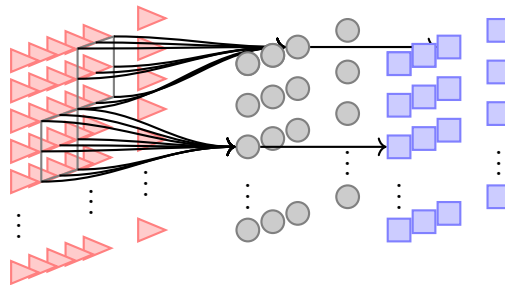


Figure 1.8: Pictorial representation of a layer of a convolutional supernode. Several supernodes might be placed side by side to form a convolutional layer.

Convolutional neural networks are nowadays widely used in image recognition with outstanding results and they improve with a steady pace. A technological application of this kind of network is the real time recognition of obstacles in a vehicle path, for safety and automation purposes in the automotive industry.

1.4.2 Other Types of NNs

By changing the topology of the nodes distribution and their connections, one obtain other networks that cannot be catalogued under the class of feedforward networks. Moreover, those different types of network are not a niche, but they are widely ?? studied as a different approaches to the same or additional problems.

Recurrent NN

Recurrent neural network are a kind of network in which a portion of the input of nodes depends on the (past) output of the same nodes or nodes of subsequent layers. That is information does not propagates only forward like in the feedforward networks, but can propagate also backward, for example in loops or in feedbacks.

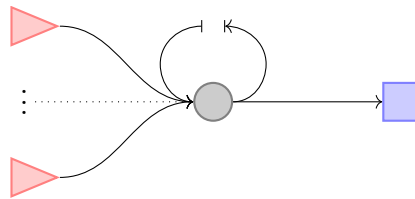


Figure 1.9: Representation of a recurrent node. One of the inputs is given by the output itself. This output to input connection could be mediated by a delay device, so that for example the output at $t - 1$ becomes the input at t . Depending on the structure of the network, there might be recurrent nodes and/or recurrent groups of nodes, i.e. loops.

Recurrent networks have found greatest use in time series analysis and prediction [18]. However often recurrent type of networks are employed to obtain the same classification of feedforward ones. In this case, the former are equivalent to the latter, if “unfolded” in time. That is the expansion of the recurrent architecture in time is the same as the topology of the feedforward one in space.

Reservoir NN

Reservoir neural networks differ from feedforward and recurrent networks in the learning approach. In fact, the topology of a reservoir network could be exactly the same as that of a deep multi-layer perceptron or that of a recurrent network. However, the reservoir computing differs in approach in respect to deep learning. It claims that it is not necessary to learn all the weights of the network, as in deep learning, but it is sufficient to train only the last (perceptron) layer of the network.

This kind of networks, then, can be trained much faster than their respective counterparts, i.e. feedforward and recurrent. The question over which training method is correct is still debated and literature does not provide clear answers yet.

1.5 ANN Simulation

In the field of artificial neural network simulation, there are several platforms that are independently developed. Among them there are TensorFlow, Theano, Caffe, Keras, Torch, and PyTorch. Unfortunately, each one of them have its strength and weakness, therefore the choice of the framework becomes very difficult.

To make a choice, the key factors considered were the language used, the features, the flexibility, and the level of diffusion of the framework in the machine learning community. The

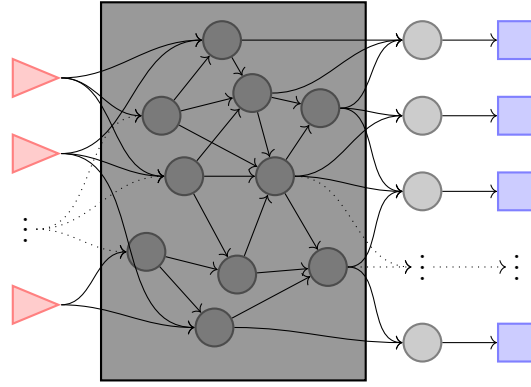


Figure 1.10: A reservoir NN is topologically equivalent to deep networks. However only the last layer is trained. In this picture the trained nodes are represented outside the box, while those inside are initialized with random weights which are then left unchanged.

language used is a determining factor, because it takes time to learn the peculiarities of a library written for a known language, but even more time to learn to use an unknown programming language. However also the features and the flexibility in the implementation are important traits, on account of the fact that any feature that is not natively implemented needs new coding. In turn, it is difficult to integrate new coding if the framework is not flexible enough to accommodate extensions or custom definitions. Last, but not least, it is easier to find support for a widespread framework in respect to a limitedly used one. In regards to this, Figure 1.11 shows the number of internet searches for some frameworks in the past few years.

In light of the facts above, PyTorch was chosen as framework. PyTorch is an open source machine learning library for python, which development has started only recently and it is based upon the older framework Torch [19]. It provides a high-level platform for the deep learning ecosystem and integrates acceleration libraries that allow fast and lean operation, both on common CPUs and GPUs. It is based on a backpropagation algorithm called *Reverse-mode auto-differentiation*, which allows versatile execution.

To summarize, the library was chosen for its language, its flexibility, and the growing interest for it within the machine learning community. Nevertheless, its features make it a very powerful framework. However, considering the need to keep the simulated system as simple as possible, this last characteristic slipped in the background. The need to simulate a simple network comes from the fact that the ultimate goal of this project is to implement an ANN with a (photonic) hardware architecture.

1.5.1 PyTorch

PyTorch is a Python package which provides a powerful framework for deep learning. It is versatile in the sense that allow customizations at almost every level of operation. For the purposes of this work, a neural network implemented in PyTorch is composed by the definition of three main components and a few lines of code to implement the operation.

The most important part of the network is the so called *model*, which defines the topology of the network by setting parameters such as the number of nodes in each layer and the connections among them. Moreover, it defines also the activation function for each node, separately or in groups. The activation function can be coded from scratch, but can also be one of the functions provided by the library or a composition of them. While the first offers almost unlimited flexibility, the second choice consents to exploit the functions already given. The second option is the best choice, if the needs of the task support it, because it allows to save much time.

Another important part of the network is the so called *criterion*, which is nothing else than

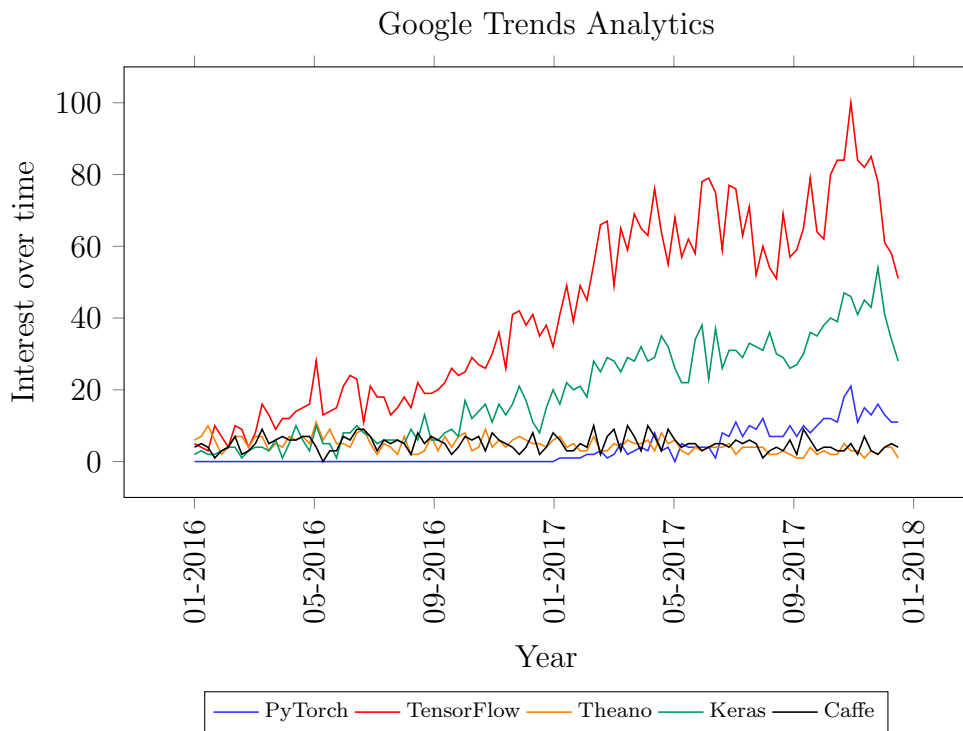


Figure 1.11: Google Search statistics for different keywords in the *machine learning and artificial intelligence* field. Numbers represent search interest relative to the highest point on the chart for the given region and time. A value of 100 is the peak popularity for the term.

the loss function. The set of functions provided by PyTorch can accommodate almost any necessity. Moreover, their operation can usually be adjusted with some internal parameters.

Similarly to the criterion, the last piece of the system is given by the *optimizer*. Optimizers are a class of algorithms that provides the optimization of the weights during the learning phase. Most commonly used methods are already supported and they provide parameters to fine tune their execution.

Following the official tutorials and the immense package documentation, I implemented a multi-layer perceptron (MLP) and then tested it with randomly generated numbers until its operation seemed correct. The model that I defined allows to implement a fully-connected feedforward neural network with some parameters. Specifically, the parameters cover the number of input and output nodes, the number of hidden layer, and the number of nodes in each hidden layer. Another degree of freedom that I implemented is whether the last hidden layer has a nonlinear activation function or a linear one. The scheme of the network is shown in Figure 1.12.

The optimizer chosen is called *Stochastic Gradient Descent* (SGD), which is parametrized just by the learning rate, at least in its vanilla implementation. The criterion used initially is the mean square error, however it was eventually replaced by the cross entropy loss (CEL), which is more suited to the classification task.

1.5.2 Dataset

Initial tests and trials on artificial neural networks are often made by using randomly generated sets of numbers. However, once the system has been successfully set up, to compare different working parameters such as number of nodes and number of layers, a common standardized dataset should be employed. Moreover in this way, it is possible to compare implementations

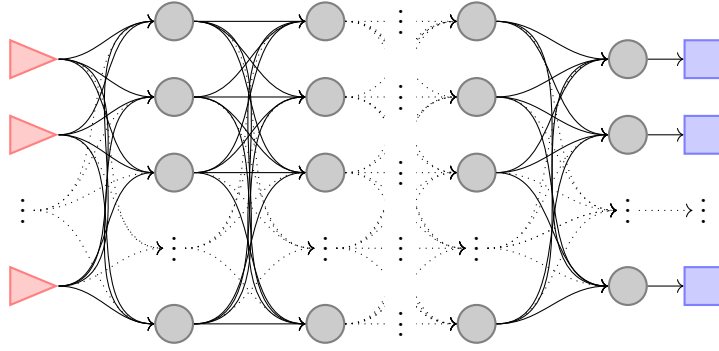


Figure 1.12: Topology of the model implemented in PyTorch. The number of input and output nodes, as well as the number of nodes in the last hidden layers is determined by the dataset. The number of nodes in the other hidden layers and the number of hidden layers itself is governed by a parameter.

belonging to other research groups.

Again, the need to keep the system as simple as possible, drove my attention towards datasets of middle to small sizes. With the help of the *UC Irvine Machine Learning Repository* [20], I selected one with a bit less than a thousand entries. The dataset is called *Connectionist Bench (Vowel Recognition - Deterding Data) Data Set*. It is composed by 990 entries of 10 attributes, i.e. input values, grouped in 11 classes.

Each entry is a vector of 10 real numbers plus an integer number between 0 and 10. In view of the fact the proposed activation function is a real-positive-valued function (see Section 3.2), I normalized the database. The normalization is independently applied to each one of the attributes in such a way that is described by a real number in $[0, 1]$. The normalization is applied before the dataset is divided in the learning and testing examples.

The authors suggest to divide the dataset a learning set of 528 entries and a testing set of 462 entries. Since the number of entries is low, compared to other datasets, the validation set is not defined. In this case, the test set is used as validation instead too.

1.5.3 Simulated ANN operation

Using the chosen dataset, I tested the neural network operation on the model defined before, with two different kinds of activation function. Initially I implemented a *ReLU* and a sigmoid activation functions. The ReLU function is a standard activation function and is defined as follows:

$$f_{ReLU}(x) = \begin{cases} 0 & \text{for } x \leq 0 \\ x & \text{for } x \geq 0 \end{cases} . \quad (1.5)$$

On the other hand, the sigmoid function, which has already been shown in Figure 1.3b, is defined by

$$f_{Logistic}(x) = \frac{1}{1 + e^{-k(x-x_0)}} , \quad (1.6)$$

with $k \in \mathcal{R}^+$ and $x_0 \in \mathcal{R}$ parameters. Both functions are widely used in literature, however the *ReLU* function seems to be preferred lately.

In Section 3.3 there are the results of the same network models, with the nonlinear activation function given by the microring resonator.

The choice of the structure of the neural network is purely heuristic. Up to now, no satisfactory method has been proposed in literature. However, given the problem (dataset), at least

the input and output layer have a fixed amount of nodes. Specifically, the input nodes are 10, the number of attributes, while the output nodes are 11, the number of classes.

Learning

The learning process with the

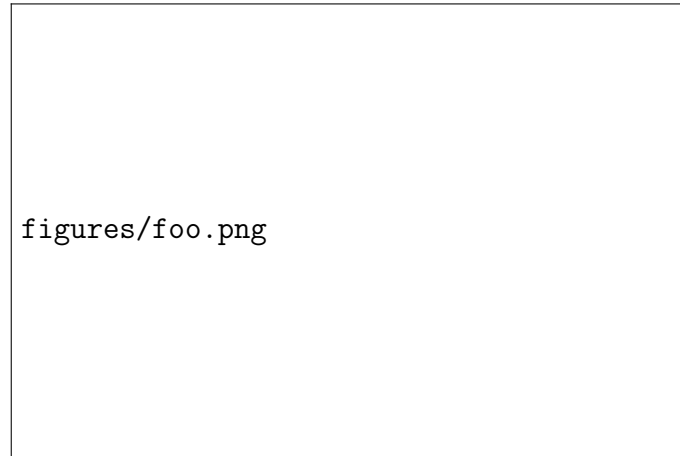


Figure 1.13: learning process

Collection of results

| no. hidden layers | no. nodes per layer | other parameters | nonlinear function | Percent correct |
|----------------------|------------------------|---------------------|-----------------------|--------------------|
| c | c | c | c | c |
| c | c | c | c | c |

Chapter 2

Integrated Photonics

Photonics is the physical science which studies detection, manipulation, and emission of light. Specifically, integrated photonics is the branch that studies how to reduce and *integrate* macroscopic optical devices in miniaturized structures.

In the past few decades, thanks to the constant improvement of the manufacturing techniques, many productive problems have been progressively resolved. Moreover interest in the field is rising, driven by the growing needs of information and communication technology (ICT), which was in turn following the increase in computational power of electronics. Many integrated devices have been proposed and some of them even commercialized [21].

2.1 Silicon Photonics

Silicon-on-Insulator (SOI) photonics is one of the widest branches of integrated photonics. It pursues the same objectives of all integrated photonics with the addition of following the production steps already developed for microelectronics.

Its framework is silicon, which is transparent in the same range of frequencies used by fiber optics. It is a the well-known material, largely studied for microelectronics, and it allow relatively easy manufacturing of high grade structures. The bulk silicon is altered by a series of often numerous production steps. The first step is the burial of an insulator layer of SiO_2 , called *buffer*, which defines the bottom surface of the layer at the top. The pure Si volume at the top, the *device* layer, is where integrated optical structures will be built with various processes like photolithography, thermal oxidation, ion implantation, and etching. A schematic representation of the layers is shown in Figure 2.1.

The fact of relying on the SOI framework to build integrated devices is a strength of silicon photonics, because it enables researchers to develop CMOS compatible integrated optical structures. Complementary Metal-Oxide-Semiconductor (CMOS) compatibility is an industry standard created to fabricate microelectronic devices. Therefore by exploiting this standard all the know-how of the manufacturing industries behind the commercial microelectronic products is available to fabricate integrated photonics devices.

Moreover, by sharing the fabrication technology with microelectronic makes it easier to integrate electronic components and obtain hybrid integrated optoelectronic devices or compensate lack of appropriate optical structures.

Hence silicon photonics is a promising technology for a combination of cost and technological reasons. A list of advantages and disadvantages of silicon photonics compared to other integrated photonics technologies is provided in Table 2.1.

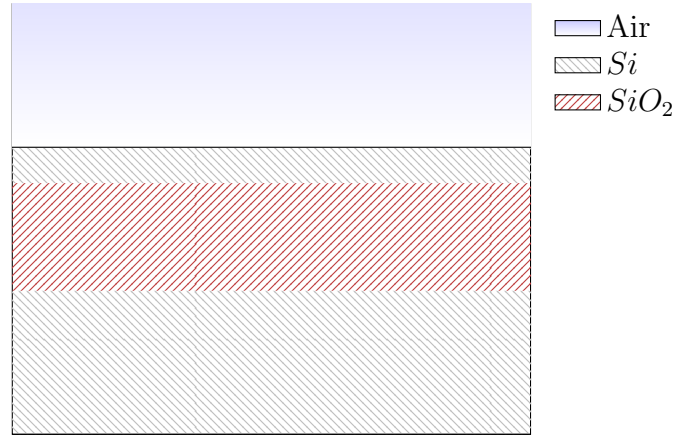


Figure 2.1: SOI productive framework. The buffer layer of SiO_2 is buried underneath the pure crystalline Si device layer which is used to build structures. The top silicon layer will become the volume in which light will be confined. The bottom silicon, underneath the buffer layer, is called substrate.

| Advantages | Disadvantages |
|--|---|
| <ul style="list-style-type: none"> i. Stable, well-understood material ii. Stable native oxide available for cladding and electrical isolation iii. Relatively low-cost substrates iv. Optically transparent at important wavelengths of $1.3\mu m$ and $1.55\mu m$ v. Well-characterized processing vi. Highly confining optical technology vii. High refractive index means short devices viii. Micro-machining means V-grooves and an effective hybrid technology are possible ix. Semiconductor material offers the potential of optical and electronic integration x. High thermal conductivity means tolerance to high-power devices or to high packing density xi. Carrier injection means optical modulation is possible xii. Thermo-optic effect means a second possibility for optical modulation exists | <ul style="list-style-type: none"> i. No Pockels effect ii. indirect bandgap means that native optical sources are not possible iii. High refractive index means that inherently short devices which are difficult to fabricate (e.g. gratings) iv. Modulation mechanisms tend to be relatively slow v. Thermal effects can be problematic for some optical circuits |

Table 2.1: Advantages and disadvantages of silicon photonics over other integrated photonics technologies. Taken from [22].

2.2 Guided-wave photonics

The most important thing for integrated photonics is the way light is confined and manipulated into microscopic structures. While in conventional optics, light is delivered with bulky mirrors and lenses toward the desired position, in integrated photonics waveguides are the main device for this task. Moreover, they are the fundamental block for building more complex devices, whether they are passive, active, or hybrid optoelectronic devices. A few illustrative devices are the waveguide coupler, the Array Waveguide Grating (AWG), the electro-optic modulators, and integrated Mach-Zehnder Interferometer (MZI).

2.2.1 Waveguides

A waveguide is a path inside a medium, whose volume is defined by a certain number of interfaces between different materials, in which light remains confined and ideally travels with negligible losses. This volume is called *core* of the waveguide, while the medium external to it, if present, is called *cladding*.

One can distinguish two types of waveguides: metallic and dielectric. The former are based on the reflection of the electromagnetic field by the metallic surface. Light is confined in the desired path by a series of metallic mirrors. However, this mechanism works well only for electromagnetic radiation for which metals can still be considered *perfect metals*. For visible and infrared frequencies integrated metallic waveguides are not possible, due to too high absorption of the metals at optical frequencies.

On the other hand, dielectric waveguides are based on the phenomenon of total internal reflection (TIR) at the interface between two dielectric media. To produce TIR, the two materials must have sufficiently different real part of the refractive index. Moreover, they must also be transparent, i.e. they must have low imaginary part of the refractive index, in the required range of frequencies. Hence not all media are suitable to build dielectric waveguides that work at a specific wavelength. For example, silicon is known to be transparent in the near infrared region.

Dielectric Waveguides

Total internal reflection is the well-known phenomenon in which light coming from a material with high refractive index n_H gets reflected at the interface with a material with low refractive index n_L . For this to happen, incident light must be at an angle greater than the critical angle given by the Snell's law:

$$\theta_C = \arcsin \left(\frac{n_L}{n_H} \right).$$

Waveguides have many shapes, however one can initially discriminate them by the dimensionality of the confinement of light. The simplest one is called *slab* and it is composed by two interfaces, which divides the material in three volumes, as shown in Figure 2.2. This type is classified as a 1D-waveguide, because it constrains light in only one dimension.

2D-waveguides on the other hand are more common, to the point that with the term waveguide one usually refers to a device belonging to this category. Since they confine light in two dimension, their core defines a path with which one can conduct light from a place to another. A few types are shown in Figure 2.3.

Obviously, the versatility of straight (2D-) waveguides is limited. Hence more complex structures such as bent waveguides have been developed.

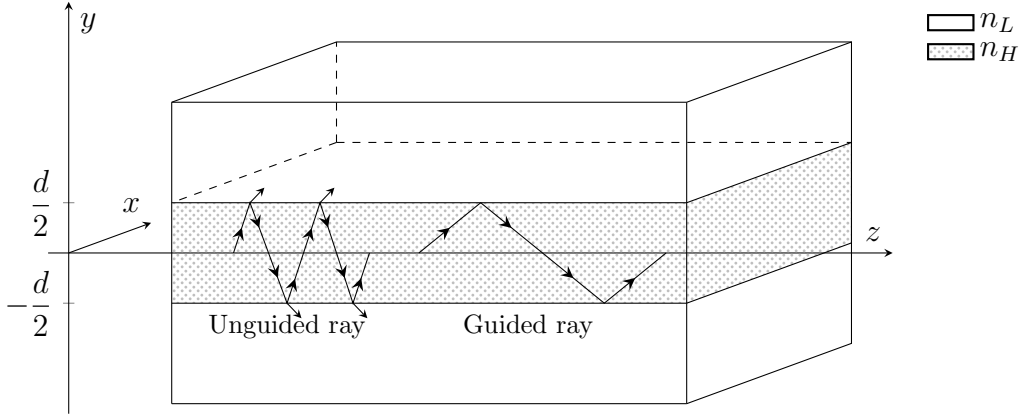


Figure 2.2: Scheme of a dielectric slab waveguide, made by two materials with refractive indexes n_H and n_L , with $n_H > n_L$. Two rays are shown: the unguided one is incident on the interface at an angle smaller than the critical angle. Conversely the guided ray is incident at a greater angle and is therefore totally reflected inside the waveguide [23].

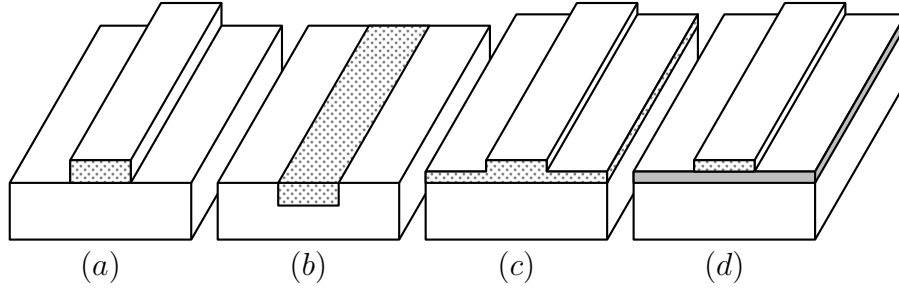


Figure 2.3: Representation of a few types of 2D dielectric waveguides. Darker areas represent higher refractive index. Light is constrained in two direction and can only move forward or backward in the third direction. (a) strip, (b) embedded strip, (c) rib, (d) strip loaded [23].

Propagation of light inside waveguides

A more complete description of guided modes is given by wave physics, where waveguides modes are described as superposition of planar transverse electro-magnetic (TEM) waves. The result of the superposition is the so called *mode*, which is expressed mathematically by

$$\phi(\mathbf{r}) = \phi_m(x, y) e^{i(\beta_m z - \omega t)}. \quad (2.1)$$

$\phi_m(x, y)$ is the transverse field distribution, z is the direction of propagation, β_m is the propagation constant of the m -th mode, and $\omega = 2\pi\nu$ is the angular frequency of light. Since light has two independent polarization, there are different modes for different polarizations. Modes are therefore separated in *transverse electric* (TE) and *transverse magnetic* (TM), which propagates differently due to geometrical asymmetries.

Each mode, identified by the m index, travels inside the waveguide with a certain propagation constant β and maintaining a field distribution ϕ_m . Both of them depend on the materials and the geometry of the waveguide. However, while β_m decrease with increasing m indexes, the features of the function ϕ_m grows in number. Light often propagates in a manner described by a mode or superposition of them. Usually other field distributions are rapidly scattered away.

The field distribution of some of the first modes, in the simplest case of a slab waveguide, is represented in Figure 2.4. The function inside the core is characterized by maxima, minima and nodes with a certain periodicity and the number of nodes is strictly linked to the index m . Outside, the distribution of the field decays exponentially. For waveguide with a 2D core,

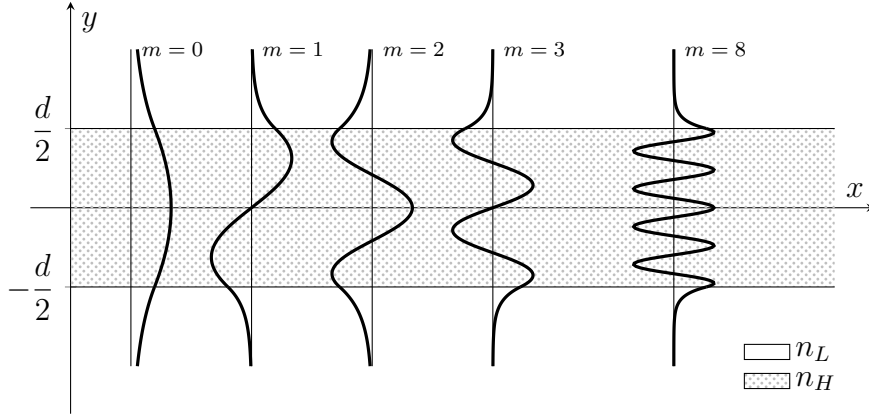


Figure 2.4: Field distribution inside a slab waveguide.

the field can be expected to be a multivariate version of similar functions. However, differently from the analytical solution for slab waveguides, they are almost always found numerically.

The propagation constant can be written as

$$\beta_m = n_{eff} k_0 + i\alpha_{eff}/2 \quad (2.2)$$

where k_0 is the wavevector in vacuum, $n_{eff} := c_0/v_{ph}$ is the *effective refractive index* of the mode, and α_{eff} is *effective absorption coefficient*. The effective refractive index is the ratio between the speed of light and the *effective phase velocity* v_{ph} at which each wavefront propagates in the core. It is a pure number and its value is between the core refractive index and the cladding refractive index $n_L < n_{eff} < n_H$. Given a WG geometry, larger n_{eff} means a greater confinement of the electromagnetic field inside the core and a slower propagation speed along the waveguide. The effective absorption coefficient instead is defined by the ratio between the input and output powers for a material of depth L , such that $I_{out}/I_{in} = e^{-\alpha_{eff}L}$, and has units of m^{-1} . A low absorption coefficient is synonym of transparency and low power absorption per unit length.

Each one of these parameters, which describe the propagation of light along the waveguide, depends both on the materials and the geometry of the core and the cladding, but also on the frequency of light. For dielectric waveguides, the fundamental mode ($m = 0$) is always supported while higher modes might not be, depending both on the waveguides and on the frequency of light. For this reason one distinguishes *single-mode* waveguides, which allow propagation for only the fundamental mode in a certain operative range of frequencies, from *multi-mode* waveguides, which allow higher order modes to propagate.

Equation (2.1) describes the propagation of a monochromatic light wave, which has ideally the same mode amplitude from $t = -\infty$ to $t = +\infty$. This is obviously not a good physical representation, as light is generated and absorbed. Eventually light is described to travel in wavepackets of finite duration, which are inherently non-monochromatic.

When light becomes non-monochromatic, the frequency dependence of the propagation constant β has to be considered. Usually, if working on a restricted range of frequencies, this dependence is characterized by a Taylor expansion at the second order.

$$\beta(\omega) \simeq \beta(\omega') + \frac{\partial\beta(\omega)}{\partial\omega} \Delta\omega + \frac{1}{2} \frac{\partial^2\beta(\omega)}{\partial\omega^2} \Delta\omega^2 \quad (2.3a)$$

$$\simeq \frac{1}{v_{ph}} \omega' + \frac{1}{v_g} \Delta\omega + \frac{1}{2} \text{GVD} \Delta\omega^2 \quad (2.3b)$$

$$\simeq \frac{n_{eff}}{c_0} \omega' + \frac{n_{eff}^g}{c_0} \Delta\omega + \frac{1}{2} \text{GVD} \Delta\omega^2 \quad (2.3c)$$

where $\Delta\omega = \omega - \omega'$ and ω' is the frequency around which β is expanded. Equation 2.3b is the same expansion, but the derivative are substituted by new quantities: the *phase velocity* v_{ph} , which describes the propagation speed of the wavefront of each frequency, the *group velocity* v_g , which describes the speed at which the ensemble of frequencies, the wavepacket, propagates, and finally the *group velocity dispersion* GVD, which describes the relative behavior of the different frequency components in a single wavepacket. Values of GVD $\neq 0$ the wavepacket will either compress or dilate in time. Those quantities are defined as follows:

$$v_{ph} := \left(\frac{\beta}{\omega'} \right)^{-1} \quad (2.4a)$$

$$v_g := \left(\frac{\partial \beta}{\partial \omega} \right)^{-1} \quad (2.4b)$$

$$\text{GVD} := \frac{\partial^2 \beta}{\partial \omega^2} = \frac{\partial}{\partial \omega} \frac{1}{v_g}. \quad (2.4c)$$

On the other hand, it could be useful to express the propagation constant in terms of the effective refractive index, where $n_{eff} = c_0/v_{ph}$. Then, similarly to the meaning of n_{eff} , one can define the *effective group index* n_{eff}^g as the ratio between the speed of light in vacuum c_0 and the effective group velocity v_g of a packet of light inside a waveguide

$$n_{eff}^g := \frac{c_0}{v_g} = n_{eff}(\omega) + \omega \frac{\partial n_{eff}}{\partial \omega} \simeq n_{eff}(\lambda) - \lambda \frac{\partial n_{eff}}{\partial \lambda}, \quad (2.5)$$

thus obtaining Equation 2.3c.

Nevertheless, our aim is to work in the quasi-static regime, i.e. to work with a time scale such that all measurable physical quantities converge to a finite value and do not show any time dependence. Thus the monochromatic wave propagation description is still a valid model, because it is a very good approximation of slowly varying and almost monochromatic waves, such as the one I will use in my experiments.

Coupling of light between waveguides

As shown in Figure 2.4, the field distribution of modes propagating inside a slab waveguide is mainly contained inside the core. However, the evanescent wave, i.e. the electromagnetic field outside the core, is non zero but decays exponentially from its value at the interface.

Evanescent coupling exploits the exponential decay of evanescent field outside the core to transfer light between two waveguides [22]. This means that when two waveguides are separated by a sufficiently small distance, the field distribution of one waveguide cannot decay sufficiently fast and instead extends itself over the core of the second waveguide. When this happens, optical power is transferred between the waveguides.

The simpler case is obtained when two parallel straight waveguides are separated by a small distance, a gap, and the field is non zero only at the input of one of them. Therefore light propagates along the waveguide, its evanescent field overlaps with the core of the second waveguide. Light is then *coupled* inside the second waveguide as it propagates along the first waveguide and power is transferred between the waveguides.

The maximum value of power transferred per unit length is determined mainly by the distance between the waveguides. The larger the gap, the lower will be its value. Moreover, the exchange of optical power is a periodic function of the propagating distance. Depending on the specific materials and on the geometry of the coupling region, a known amount of light can be coupled between the waveguides.

2.2.2 Microring optical cavity

In integrated photonics the microring is an optical cavity made by bending a waveguide on itself. To insert light into the cavity, the microring is often side coupled with one or two straight waveguides. Light inserted from the different ports into the cavity interfere with itself, after a round trip. When the waves are in phase, they generate constructive interference and the energy stored in the cavity increases exponentially. On the other hand, when the signals are out of phase, the interference is destructive and no energy is stored in the cavity.

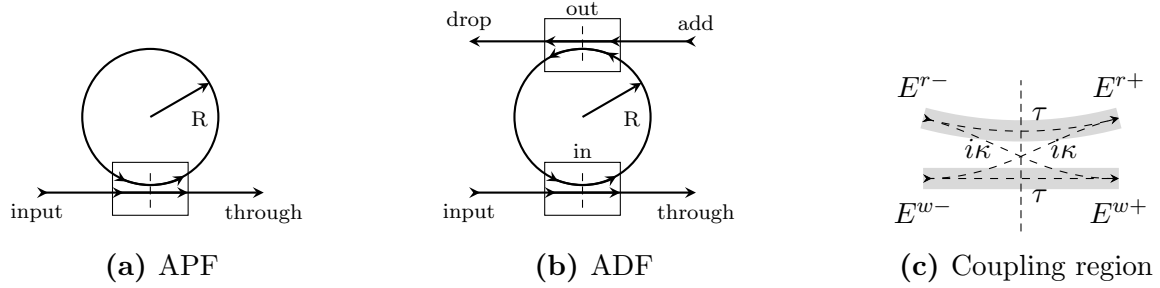


Figure 2.5: Schematic representation of microring configurations and of their coupling regions. APF has two channels, *input* and *through*, and one coupling region. ADF has four channels, *input*, *through*, *add* and *drop*, and two coupling regions. The coupling constants (κ and τ) are in principle different for each coupling region.

In the simpler case when there is only one waveguide side coupled to the resonator the optical cavity has only two ports, which are usually called *input* and *through*. This configuration, shown in Figure 2.5a, is called *All-Pass Filter*, because in the ideal case, where no losses happen, all the signal passes from the input to the through channels.

By adding a secondary waveguide coupled to the ring, one obtains the so called Add-Drop Filter (ADF) configuration, shown in Figure 2.5b. Its name derives from the fact that the two additional ports are called *add* and *drop* respectively. This simple structure can be readily used as a signal mixer: signals at the resonance wavelengths of the cavity are directed from the input to the drop channel or from the add channel to the through port. Additionally signals out of resonance travel straight from the input to the through channel and from the add to the drop port.

In both configurations light is transferred from the waveguides to the microring within the *coupling regions*, as shown in Figure 2.5c. The simplest model considers the region as infinitely small compared to the other dimensions. However the model can be expanded to include coupling regions with a finite length, which transform the microring in the so called *racetrack resonator*.

The theoretical model usually employed to describe resonators analytically decomposes their structure in a series of simpler substructures. Both the APF and the ADF configurations are studied as ordered combinations of straight waveguides, coupling regions, and bent waveguides. Other used descriptions, such as numerical simulation obtained with finite element methods (FEM), achieve more precise results, however they are more dependent on the specific geometry of the problem. Moreover the approximation given by the analytical model is sufficiently accurate to make quantitative prediction of the coupling and it gives a clear description of the physics behind it. Furthermore it can be expanded to include non-trivial phenomena (see Section 2.3). In the following section I will go through the necessary steps to solve the case of the ADF configuration in the theoretical model.

Add-Drop-Filter theory

ADF configuration is obtained when a microring is coupled to two waveguides. Such structure is composed by three different basic structures: four straight waveguides, two bent waveguides which together form the whole ring, and two coupling regions between the waveguides and the microring. Each of these pieces transfers light to or from the outside or another piece.

Since our experiments are carried out in a time scale such that physics phenomena can be considered quasi-static, the field propagating in the device is described by a scalar complex function which, assuming a monochromatic continuous EM wave, loses any temporal dependence:

$$E(z) = |E(z_0)|e^{i\beta z}, \quad (2.6)$$

where z is the direction of propagation, loosely defined to accommodate propagation both along straight and bent waveguides ($z \sim r\theta$), t is time, $\omega = 2\pi\nu$ is the angular frequency, and $\beta = n_{eff}k_0 + i\alpha_{eff}/2$ is the propagation constant. Both dependence of the effective index $n_{eff} = n_{eff}(\omega)$ and the effective loss factor $\alpha_{eff} = \alpha_{eff}(\omega)$ will be expanded only when necessary.

Generally the propagation along the straight waveguides is considered lossless (i.e. $\alpha_{eff} \approx 0$), while the propagation along the two bent regions has a non negligible loss (i.e. $\alpha_{eff} > 0$). The coupler between the resonator and the waveguides is considered like a beamsplitter. In this approximation, light does not propagate in this part as it was in the previous ones. Its operation is reduced to the exchange of power between the two input ports and two output ports, which is described by the following matrices:

$$\begin{pmatrix} E_{ch}^{w+} \\ E_{ch}^{r+} \end{pmatrix} = \mathbf{M} \begin{pmatrix} E_{ch}^{w-} \\ E_{ch}^{r-} \end{pmatrix}, \quad \mathbf{M} = \begin{pmatrix} \tau & i\kappa \\ i\kappa & \tau \end{pmatrix}, \quad (2.7)$$

where E is the field amplitude of the ‘ $_{ch}$ ’ channel either in the waveguide ‘ w ’ or in the ring ‘ r ’, before ‘ $-$ ’ and after ‘ $+$ ’ the coupling. An explanatory diagram is shown in Figure 2.5c. The matrix \mathbf{M} is characterized by two real valued parameters, τ and κ , between 0 and 1. Specifically, they must verify the following constraint:

$$\det(\mathbf{M}) = |\tau|^2 + |\kappa|^2 = 1. \quad (2.8)$$

which represents the conservation of energy.

At this point one can solve the problem by putting all the pieces together. Neglecting the propagation inside the waveguide, the full system of equation that describe the problem is:

$$E_{in}^{w+} = \tau E_{in}^{w-} + i\kappa E_{in}^{r-} \quad (2.9a)$$

$$E_{in}^{r+} = i\kappa E_{in}^{w-} + \tau E_{in}^{r-} \quad (2.9b)$$

$$E_{out}^{r-} = E_{in}^{r+} e^{i\beta\pi R} \quad (2.9c)$$

$$E_{in}^{r-} = E_{out}^{r+} e^{i\beta\pi R} \quad (2.9d)$$

$$E_{out}^{w+} = \tau E_{out}^{w-} + i\kappa E_{out}^{r-} \quad (2.9e)$$

$$E_{out}^{r+} = i\kappa E_{out}^{w-} + \tau E_{out}^{r-} \quad (2.9f)$$

The first two equations (2.9a) and (2.9b) describe the exchange of optical power between the first channel and the microring resonator (see *in* box in Figure 2.5b). Then the third and fourth equations (2.9c) and (2.9d) delineate the propagation of light in the two halves of the resonator, from one coupling region to the other. Lastly the remaining two equation

characterize the transfer of light between the resonator and the add-drop channel (see *out* box in Figure 2.5b).

Using these equations it is easy to define new quantities of interest: the first one is the transmittance from the *input* to the *through* port.

$$\eta_T(\omega) := \frac{E_{in}^{w+}}{E_{in}^{w-}} = t \frac{1 - e^{i\beta 2\pi R}}{1 - \tau^2 e^{i\beta 2\pi R}} \quad (2.10)$$

Similarly, one can also define the transmittance from the *input* to the *drop* port.

$$\eta_D(\omega) := \frac{E_{out}^{w+}}{E_{in}^{w-}} = \frac{-\kappa^2 e^{i\beta \pi R}}{1 - \tau^2 e^{i\beta 2\pi R}} \quad (2.11)$$

However, these quantities have complex values and therefore are difficult to study. For this reason, one usually defines the transmission between the same ports as the square modulus of the transmittance. Thus it follows that

$$T(\omega) := |\eta_T|^2 = \tau \frac{(1 - \gamma)^2 + 4\gamma \sin^2(n_{eff} k_0 \pi R)}{(1 - \tau^2 \gamma)^2 + 4\tau^2 \gamma \sin^2(n_{eff} k_0 \pi R)} \quad (2.12)$$

and

$$D(\omega) := |\eta_D|^2 = \frac{\kappa^4 \gamma}{(1 - \tau^2 \gamma)^2 + 4\tau^2 \gamma \sin^2(n_{eff} k_0 \pi R)} \quad (2.13)$$

where the notation is simplified by loss parameter $\gamma = e^{-\alpha_{eff} \pi R}$. The dependence of $T = T(\omega)$ and $D = D(\omega)$ from the frequency (or wavelength) of light is obtained by making explicit the wavevector dependence $k_0 = \frac{\omega}{c_0} = \frac{2\pi}{\lambda}$ in which c_0 is the speed of light in vacuum.

Apart from a simpler description, transmission is directly connected with the optical power as it represents the ratio between the input and output power. In fact, the optical power is defined as the square modulus of the optical field, except for a constant factor:

$$I = \frac{1}{2} n_0 c_0 |E|^2 \propto |E|^2$$

Both transmission spectra, as shown in Figure 2.6, have either peaks or dips: at each microring resonance, the through spectrum shows dips while the drop spectrum shows peaks. The depth of the dips, the height of the peaks, and the width of both of them is defined by few parameters: the coupling constant τ^1 and the half round trip loss factor $\gamma = e^{-\alpha_{eff} \pi R}$.

The frequency of each resonance is identified by a positive integer number, that verifies the following equation:

$$\omega_m = m \frac{c_0}{n_{eff}(\omega) R}, \quad (2.14)$$

where the dependence of $n_{eff} = n_{eff}(\omega)$ has been explicitly shown.

Each resonance is spaced from the next one by a quantity called *Free Spectral Range* FSR_{ω_m} . By exploiting the Taylor expansion of β seen in equation (2.3c) one obtains

$$FSR_{\omega_m} \simeq \frac{c_0}{n_{eff}^g(\omega_m) R}. \quad (2.15)$$

where the *effective group index* $n_{eff}^g(\omega)$ has been defined in equation (2.5). Another important quantity is the width of the peaks or dips of each resonance. Ordinarily one evaluates the so called *full-width-half-maximum* (FWHM) of the transmission in the drop channel:

$$FWHM_{\omega_m} = \frac{c_0}{n_{eff}^g(\omega_m)} \frac{1 - \tau^2 \gamma}{\pi R \tau \sqrt{\gamma}} \quad (2.16)$$

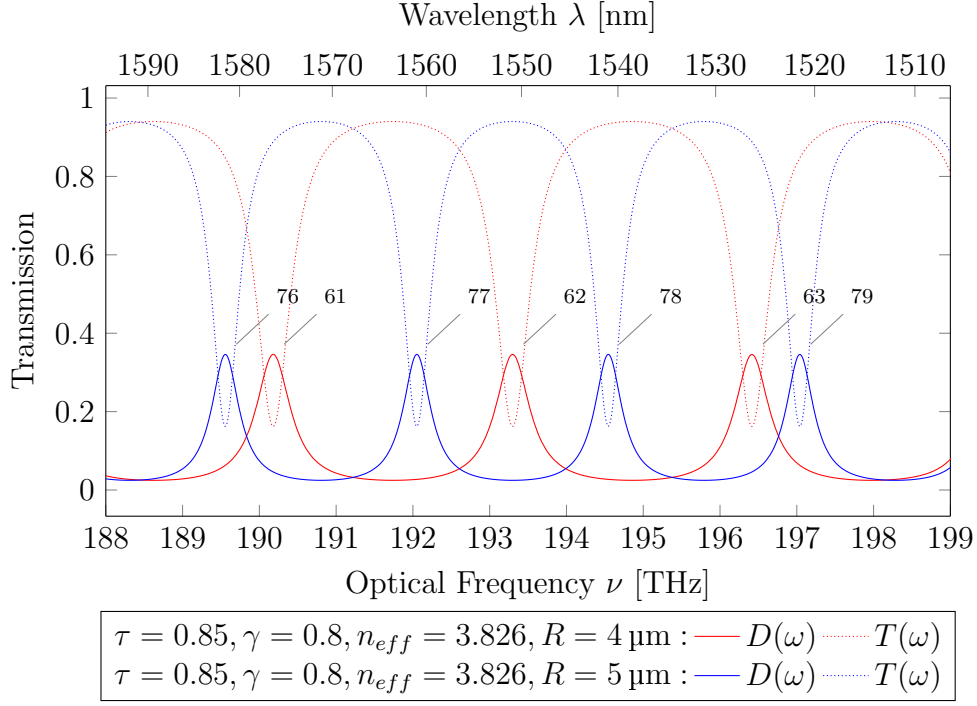


Figure 2.6: Transmission spectra of microring resonators in ADF configuration for the through $T(\omega)$ and drop ports $D(\omega)$. The resonators considered differ in radius ($R=4\mu\text{m}$ and $R=5\mu\text{m}$), but share the coupling constant $\tau=0.85$, the half round trip loss factor $\gamma=0.8$ and the effective index $n_{eff}=3.826$.

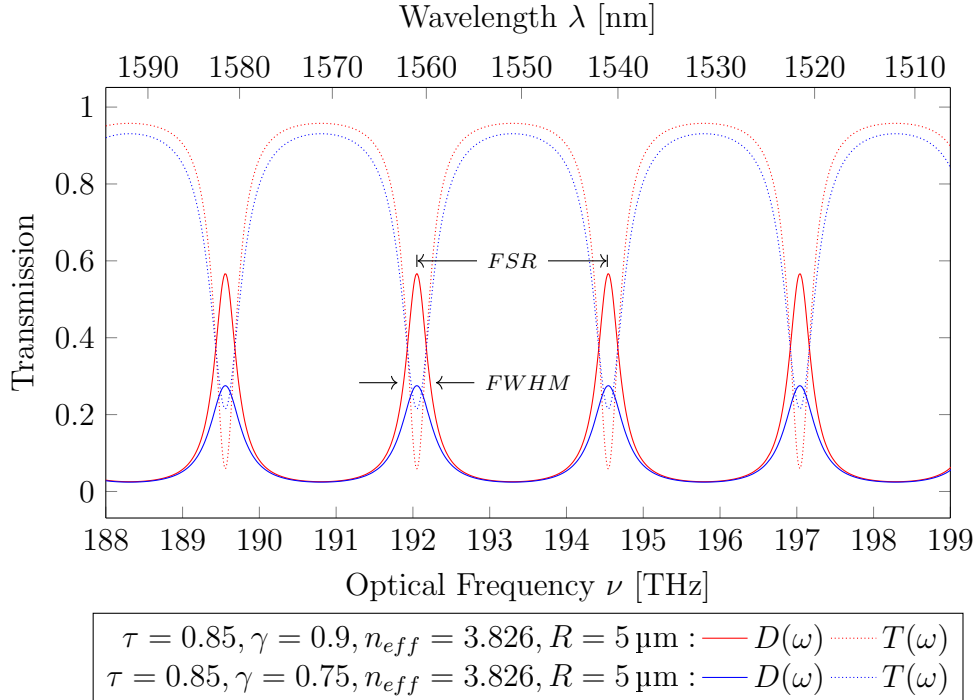


Figure 2.7: Transmission spectra of microring resonators in ADF configuration for the through $T(\omega)$ and drop ports $D(\omega)$. The microring has radius $R=5\mu\text{m}$ and effective index $n_{eff}=3.826$. The coupling constant is $\tau=0.85$, while the loss factor γ takes two values: 0.9 (red) and 0.75 (blue). The arrows indicate a $FSR_\nu \approx 2.49\text{ THz}$ and a $FWHM_\nu \approx 0.35\text{ THz}$, which gives a quality factor of around $Q \approx 550$. The blue curve has $FWHM_\nu \approx 0.5\text{ THz}$ and $Q \approx 390$. Each resonance is identified by its positive integer number.

Figure 2.7 shows both the *FSR* and the *FWHM* for a family of resonances.

Values such this are often expressed in the wavelength domain:

$$FSR_{\lambda_m} \simeq \frac{\lambda_m^2}{n_{eff}^g(\lambda_m) 2\pi R} \quad \text{and} \quad FWHM_{\lambda_m} \simeq \frac{\lambda_m^2}{n_{eff}^g} \frac{1 - \tau^2 \gamma}{2\pi^2 R \tau \sqrt{\gamma}} \quad (2.17)$$

where $n_{eff}^g(\lambda_m)$ is the appropriate redefinition of the effective group index in the wavelength domain, shown in equation (2.5).

Another important quantity to describe an optical resonator response is the *enhancement factor* EF . It is defined as the ratio between the incident optical power I_{inc} and the power circulating inside the cavity I_{ins} :

$$EF := \frac{I_{int}}{I_{inc}} \simeq \frac{|E_{in}^{r+}|^2}{|E_{in}^{w-}|^2} = \frac{\kappa^2}{(1 - \tau^2 \gamma)^2 + 4\tau^2 \gamma \sin^2(n_{eff} k_0 \pi R)}, \quad (2.18)$$

where in the last equality, I assumed low loss waveguides $\gamma \rightarrow 1$. This assumption allows to consider the field at an arbitrary position along the ring.

Finally, an additional figure of merit is the important quantity is the *quality factor* Q – *factor*, or simply Q . It has many similar definitions, depending on the field of study. The most physical, but less operative one defines Q as 2π times the ratio between the energy stored in the cavity and the energy lost each cycle.

$$Q := 2\pi \times \frac{\text{energy stored}}{\text{energy lost per cycle}} \quad (2.19)$$

However, for my purposes this definition is too cumbersome, thus I used a similar one instead:

$$Q := \frac{\omega_m}{FWHM_{\omega_m}} = \frac{\lambda_m}{FWHM_{\lambda_m}} \quad (2.20)$$

Both are sensible definitions and as Q becomes larger they become approximately equivalent.

Physically, the quality factor is linked to the photon lifetime in cavity t_m by the relation

$$Q \simeq \frac{\omega_m}{FWHM_{\omega_m}} \propto \omega_m t_m. \quad (2.21)$$

From this description one can observe that higher quality factors mean longer photon lifetimes. This is due to the fact that the photon lifetime is strictly dependent on the losses of the cavity and the Q factor is inversely related to them. However, in an optical cavity losses are given by absorption, but also by the coupling of the input and output channels. Thus, given a certain waveguide loss (defined by both the propagation and radiative contributions), the same Q -value can be obtained by different sets of loss factors. One can identify three distinct regimes: over-coupling, critical-coupling, and under-coupling regimes. Figure 2.8b shows contour plots of the maximum transmission in the drop channel and the quality factor as functions of the cavity losses (γ) and the coupling coefficients ($\kappa^2 = 1 - \tau^2$).

Coupling regimes

Microring resonator and more in general optical cavities are able to store very large quantities of optical energy. This energy, however, is continuously removed by the cavity in two main ways. The first one is the coupling mechanism between the waveguides and the microring, characterized by κ and τ , with extract light from the cavity in the same way that injects

¹one can choose also κ , but it does not matter which one, since $\tau^2 = 1 - \kappa^2$

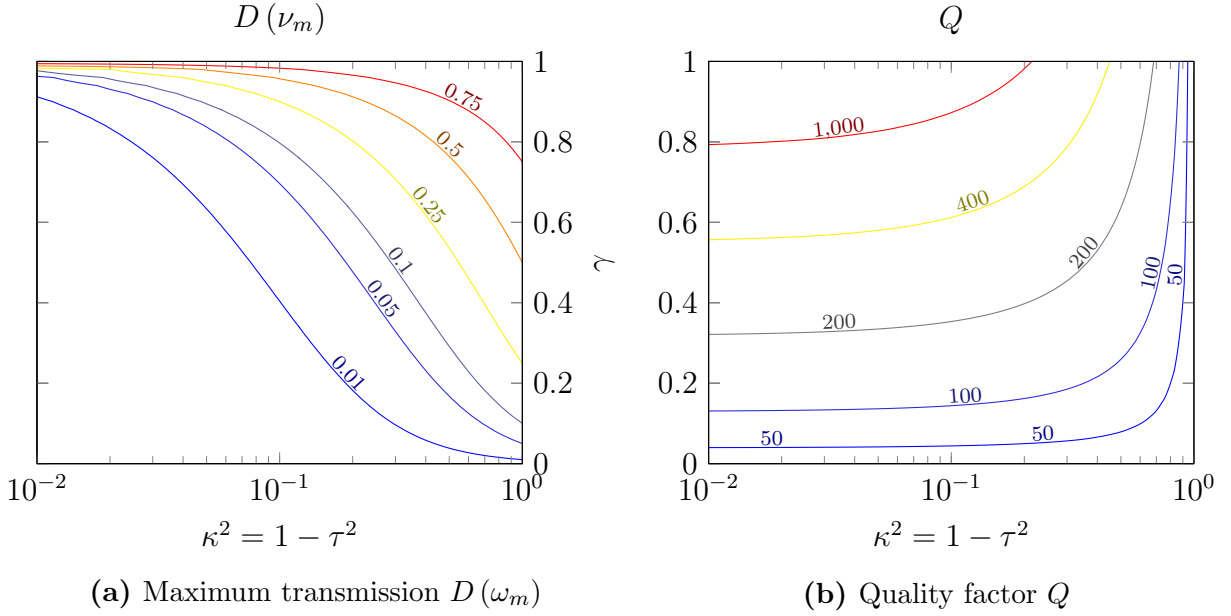


Figure 2.8: Contour plots of the maximum transmission on the drop channel $D(\omega_m)$ and of the quality factor Q , parametrized for the coupling coefficient τ^2 and the half round trip loss factor γ . The Q -factor is obtained for a resonance near $\nu_m \approx 200$ THz (arbitrarily chosen) and an effective group index $n_{eff}^g \approx 4$.

the input signals in it. The second one is the intrinsic loss, described by the half round trip loss factor γ , which in turn is composed by absorption of the material and radiative induced scattering. Absorption loss is a given property of the material, whereas radiative scattering is linked to the roughness of the surfaces and the presence of imperfections.

The quality factor can be written as

$$\frac{1}{Q_{tot}} = \frac{1}{Q_{intr}} + \frac{1}{Q_{coupl}} \quad (2.22)$$

where Q_{coupl} is dependent on the geometry and the material, whereas Q_{intr} is dependent on the quality of the manufacturing processes.

A microring resonator in the ADF configuration has two coupling regions and therefore in principle we can have symmetrical or asymmetrical coupling mechanisms. I shortly address here the case of asymmetric coupling ($\tau_1 \neq \tau_2$) to define the three coupling regimes. The coupling constants κ_i and τ_i and the loss factor γ can add up in different ways to obtain the same quality factor. Specifically, when $\tau_1 = \gamma^2 \tau_2$ is verified, the resonator is in the *critical-coupling regime*. In this particular condition, which requires asymmetrical coupling, the transmission on the through channel at the resonant frequencies goes to zero and $Q = Q_{intr}/2$. The values of the parameters for which this condition is verified split the space of parameters in the other two regimes. When $\tau_1 < \gamma^2 \tau_2$, and $Q > Q_{intr}/2$, the resonator is in *under-coupling regime*, while for $\tau_1 > \gamma^2 \tau_2$, and $Q < Q_{intr}/2$, it is in *over-coupling regime*. In both cases, the transmission on the through channel is always greater than zero.

2.3 Nonlinear Optics

In the previous section, the material of waveguides and resonators have been considered as media with linear response to electromagnetic radiation. This is, however, only an approximation, because any dielectric material shows nonlinearities if probed with a high enough electromagnetic field.

In integrated photonics, due to the lateral confinement of the field inside the waveguide, much higher field amplitude is reached in comparison to free space. Moreover, inside an optical cavity, the field reaches even more higher amplitudes thanks to its large enhancement factor and nonlinearities might arise.

Despite silicon shows a small third order nonlinear refractive index, significant nonlinear responses are obtained through a proper microresonators optical design.

One can distinguish two kinds of optical nonlinearities: electronic nonlinearities and thermal nonlinearities.

2.3.1 Electronic nonlinearities

When electromagnetic radiation propagates inside a dielectric, atoms become polarized. This polarization is usually considered linear, because the applied fields are normally weak in comparison to the inter-atomic electric fields. However, when they grow sufficiently large, e.g. 10^5 to 10^8 V m^{-1} [23], the relation between the total polarization vector and the applied optical field becomes nonlinear. Then the following generalized equation is used instead:

$$\mathbf{P} = \varepsilon_0 \left(\chi^{(1)} + \chi^{(2)} : \mathbf{E}\mathbf{E} + \chi^{(3)} : \mathbf{E}\mathbf{E}\mathbf{E} + \dots \right) \quad (2.23)$$

which in principle is a vectorial relation, where the j -th order susceptibility term $\chi^{(j)}$ is a tensor of rank $j + 1$ [24]. Often, the spatial dependences simplify and the equation can be reduced to be scalar only. This is the case of linearly polarized TEM waves, when the electric field is directed only along one direction.

Equation 2.23 allows to expand the definition of refractive index and absorption coefficient to:

$$\left(n + i \frac{c_0}{2\omega} \alpha \right)^2 = 1 + \chi \simeq 1 + \chi^{(1)} + \chi^{(2)} E^2 + \chi^{(3)} E^3 + \dots, \quad (2.24)$$

where the vectorial form has already been reduced to the scalar one.

Silicon is a centrosymmetric material and thus does not exhibit optical nonlinearities of even orders, i.e. $\chi_{Si}^{(2)} = 0$. The lowest order nonlinear effects in silicon belong to the third order $\chi_{Si}^{(3)} \neq 0$. In this category - third order nonlinearities - two are the fundamental effects that modifies the refractive index and the absorption coefficient.

Kerr effect

The Kerr effect is given by the real part of the third order nonlinear susceptibility $\chi^{(3)}$ and it produces a change in the refractive index characterized by:

$$\Delta n_{Kerr} \simeq n_2 I, \quad (2.25)$$

where I is the intensity of light beam and n_2 is the second-order (or intensity dependent) nonlinear refractive index, defined by

$$n_2 = \frac{3}{4\varepsilon_0 c_0} \text{Re} [\chi^{(3)}] \stackrel{Si}{\simeq} 0.45 \times 10^{-17} \text{ m}^2 \text{ W}^{-1}. \quad (2.26)$$

The value of n_2 is verified for light at $\lambda = 1.54 \mu\text{m}$ in silicon [25].

Two photon absorption

The other fundamental effect is the two photon absorption (TPA), which is linked instead to the imaginary part of the third order nonlinear susceptibility. It does not produce a change to the refractive index but to the absorption coefficient instead.

$$\Delta\alpha_{TPA} = \beta_{TPA}I, \quad (2.27)$$

where β_{TPA} is the TPA coefficient which is experimentally found to be [25]

$$\beta_{TPA} = \frac{3}{2\varepsilon_0 c_0^2 n^2} \text{Im} [\chi^{(3)}] \stackrel{Si}{\simeq} 0.79 \times 10^{-11} \text{ m W}^{-1}. \quad (2.28)$$

As a consequence to the absorption of two photons, a free carrier is generated in the conduction band of silicon. The presence of free carriers alters both the refractive index and the absorption coefficient.

2.3.2 Charge carrier nonlinearities

When free carriers are generated in the conduction band, they can either move around until they thermalize or they can absorb an incoming photon. The first case is the *free carrier dispersion* (FCD) effect, which affects the refractive index. The second case is the *free carrier absorption* (FCA) effect and affects the absorption coefficient. Both effects are usually characterized as first order expansions, as follows:

$$n(N) = n(N_0) + \left. \frac{dn}{dN} \right|_{N_0} \Delta N \quad (2.29)$$

$$\alpha(N) = \alpha(N_0) + \left. \frac{d\alpha}{dN} \right|_{N_0} \Delta N \quad (2.30)$$

where the value of the FCD and FCA coefficients are [22], [26]

$$\left. \frac{dn}{dN} \right|_{N_0} \stackrel{Si}{\simeq} -1.73 \times 10^{-21} \text{ m}^3 \quad \text{and} \quad \left. \frac{d\alpha}{dN} \right|_{N_0} \stackrel{Si}{\simeq} 1.1 \times 10^{-15} \text{ m}^2 \quad (2.31)$$

respectively, and ΔN is the variation in free carrier population per volume. The free carrier dynamics is usually defined as

$$\frac{d\Delta N}{dt} = -\gamma_{FC}\Delta N + G \quad (2.32)$$

where γ_{FC} is the empirical population loss factor and G is the total generation rate per unit volume [27]. The generation rate G is defined as

$$G = \frac{P_{abs}^{TPA}}{2\hbar\omega V_{ring}} \quad (2.33)$$

In our case the free carrier are mainly generated by the two photon absorption process, hence G is linked to the power absorbed by the material by the TPA effect only. Therefore the absorbed power can be explained as a function of optical power:

$$P_{abs}^{TPA} = A(1 - \gamma_{TPA}^2)I \simeq A2\pi R \Delta\alpha_{TPA}I = V\Delta\alpha_{TPA}I \quad (2.34)$$

where $A = V/2\pi R$ is the area of the microring.

2.3.3 Thermal nonlinearities

The optical nonlinearities of the refractive index due to the changes in a material being heated is called *thermo-optic effect* (TOE). This happens when heat source is, for example, a resistance, but also when light propagates inside a medium, because a portion of the photons is absorbed. To characterize this change in the refractive index caused by the temperature, a first order expansion is usually made:

$$n(T) = n(T_0) + \left. \frac{dn}{dT} \right|_{T_0} \Delta T, \quad (2.35)$$

where $\frac{dn}{dT}$ is called *thermo-optic coefficient* and ΔT is the temperature shift.

The thermo-optic coefficient (TOC) of silicon at 300 K is ?? :

$$\left. \frac{dn}{dT} \right|_{300 \text{ K}} = 1.86 \times 10^{-4} \text{ K}^{-1}. \quad (2.36)$$

Moreover, due to the fact that in silicon integrated structures the cladding is usually made by SiO_2 , a thermally insulating material, the heat generated by the beam confined in the cavity will stay within the core, thus amplifying the effect even further.

The temperature dynamics of a silicon microring resonator is driven by the optical power absorbed and by the heat lost to the surrounding medium. Specifically the Fourier law reads

$$\frac{d\Delta T(t)}{dt} = -\gamma_{TH}\Delta T(t) + \frac{P_{abs}}{M_{ring}C_p} \quad (2.37)$$

where M_{ring} is the mass of the microring, C_p is the heat capacity at constant pressure of silicon, and γ_{TH} is a phenomenological quantity which describes the heat loss rate.

$$P_{abs}^{tot} = A(1 - \gamma^2)I \simeq V(\alpha + \Delta\alpha_{TPA} + \Delta\alpha_{FCA})I \quad (2.38)$$

The power absorbed is caused both by linear and nonlinear processes. Hence the total value is given by the linear absorption coefficient α , and by the nonlinear shift of absorption coefficient produced by the two photon absorption $\Delta\alpha_{TPA}$ and by the free carrier absorption $\Delta\alpha_{FCA}$.

2.3.4 Nonlinear perturbation of microring response

When applied to the response of a microring resonator, the optical nonlinearities are particularly effective because of the enhancement factor of the cavity. Not all nonlinearities alter the behavior of the optical resonator in the same way. From the point of view of timescales, the fastest effects are the electronic and free carrier effects. Nonlinear responses given by such effects reach a steady state in less than 1 ps for the first and 1 ns for the second. On the contrary, the timescale of thermal perturbations is of the order of the 1 μ s. Each one of these values, however, depends strictly on the geometry of the structure.

On the other hand, also the magnitude of the different effects plays an important role. Having similar effects on the refractive index, at short timescales Kerr and FCD win over the thermal one, however, at longer timescales the thermal effect is the predominant one. Hence ultrashort light pulses would have shown a completely different dynamics than the one described in this thesis..

In this discussion I will consider only the sum of all effects at steady state and the thermo-optic effect is the prevalent effect at medium-high intensities, as shown in Figure 2.9.

When injecting light into a resonator, its transfer function ultimately depends on two factors: the frequency of the light compared to the frequency of the resonance and the optical power

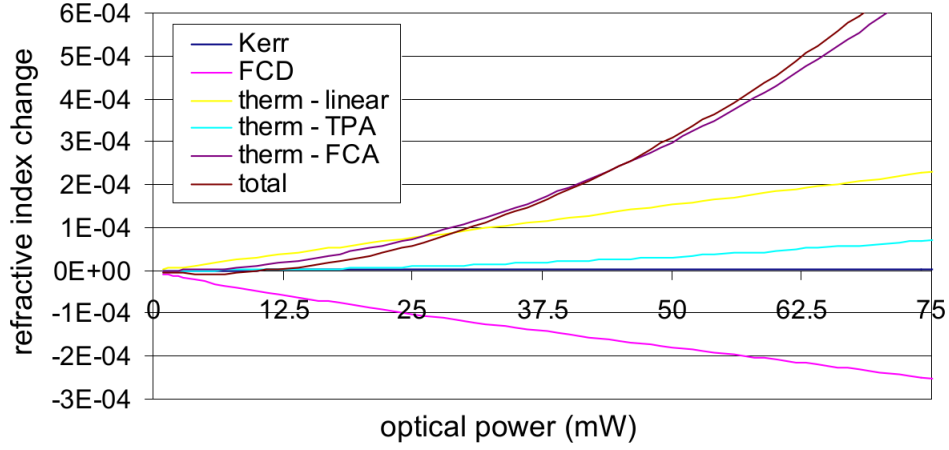


Figure 2.9: Nonlinear contributions to the refractive index change inside the ring resonator as function of the cavity power, taken from [28].

injected. At low intensities the response of a microring to frequencies around its resonance is symmetrical, as was shown in the preceding section. At higher intensities, however, the nonlinear phenomena change the refractive index of the material so much that the resonance frequency shifts. Not all nonlinear mechanisms act in the same way: for example, thermal and FCD phenomena have opposed and competing effects, which shift the resonance in opposite directions. However, as already stated, on long timescales thermal nonlinearities predominates over all the others. Hence, after the system has reached the quasi-static regime, as the intensity of the input beam grows, the cavity heats up and the refractive index increases. This produces a shift of the *cold* resonance towards smaller frequencies, as shown in Figure 2.10.

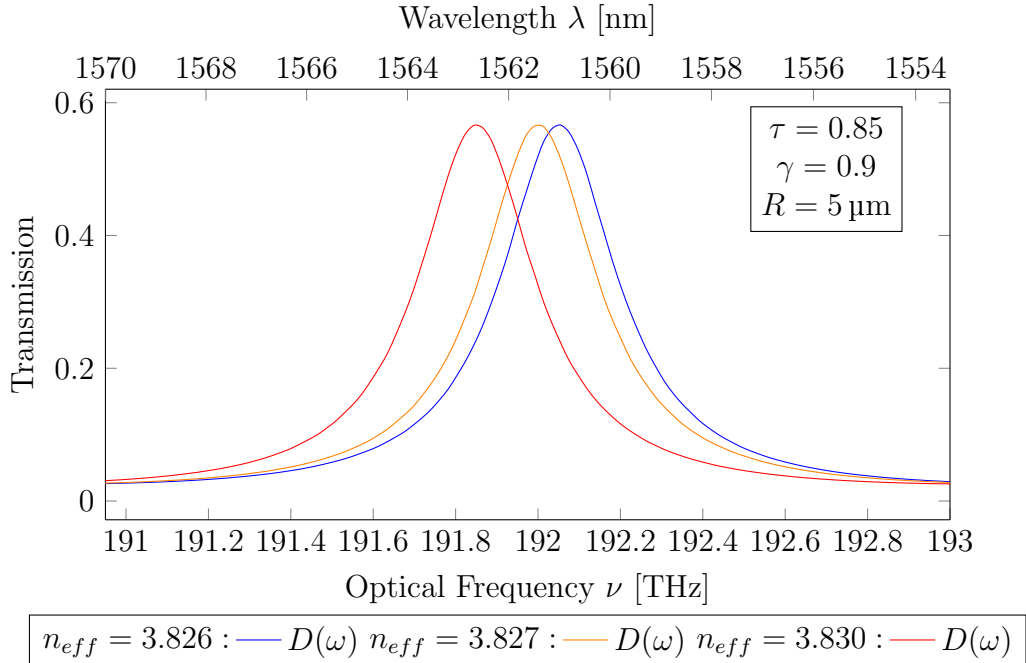


Figure 2.10: Microring resonator optical response in three different conditions: unaltered (blue), slightly increased $\Delta n = 1 \times 10^{-3}$ (orange), and substantially increased $\Delta n = 1 \times 10^{-2}$ refractive index (red). Both changes simulates the nonlinear effect of (mostly) thermal nonlinearities.

This means that by injecting a certain (high) optical power at higher frequency than the resonance frequency, or on the blue shoulder of the resonance, the obtained transmission will

be higher than the one described by the linear equations. On the other hand, by injecting the same amount of optical power at lower frequency, or on the red shoulder of the resonance, the resulted transmission will be lower than the one described by the linear equations.

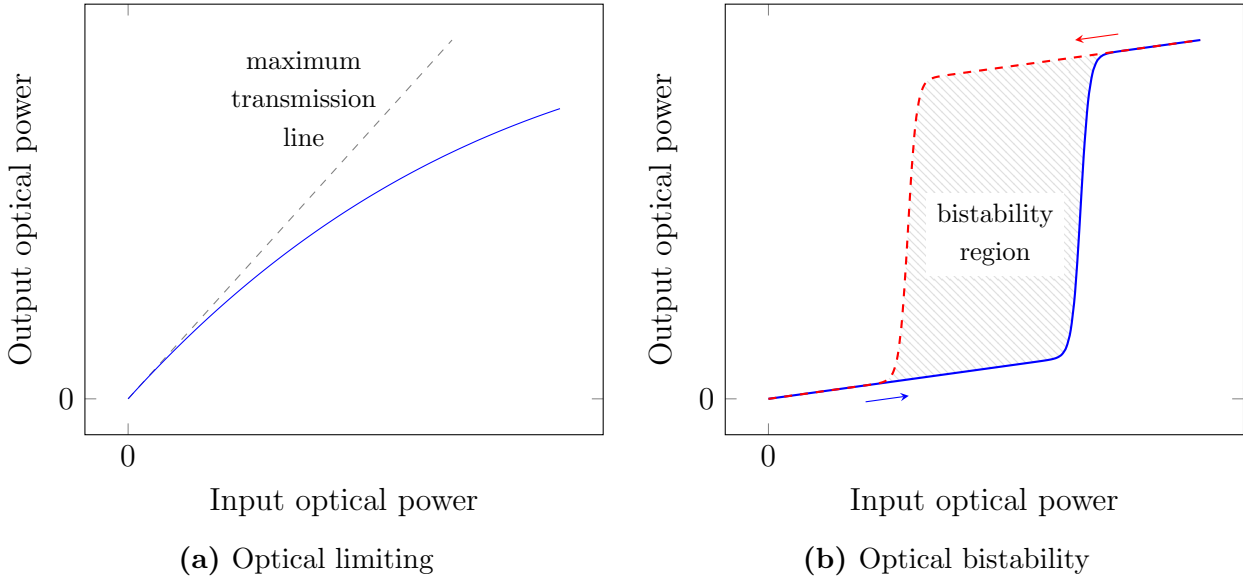


Figure 2.11: Examples of (a) optical limiting and (b) optical bistability. These curves are just a qualitative example of the phenomena. More accurate representation will be shown in the Subsection 2.4.3.

These features can be exploited to obtain two different effects. By choosing a signal with a fixed frequency on the blue shoulder of the *cold* resonance, the effect obtained is *optical limiting*. Optical limiting is the progressive decrease in transmission with the increase of the input signal. Hence, the effective transmission produced is nonlinearly dependent on the value of the input signal, as shown in Figure 2.11a. On the other hand, by choosing a signal on the red shoulder of the *cold* resonance, the effect obtained is *optical bistability*. Optical bistability is the existence of two distinct steady states of the transmission function for the same interval of input signals. In an optical microring resonator this produces abrupt *jumps* from one steady state to the other, when at the edges of such intervals. Specifically, at the right edge of the bistability region, the system switches from the lower to the higher transmission state, whereas at the left edge, the system switches from the higher to the lower transmission state. Moreover, the state inside the bistability interval is determined by the past states of the optical cavity. This defines a hysteresis cycle around the bistability region. All these features are shown in Figure 2.11b.

2.4 Integrated photonics applied to ANNs

Even though the vast majority of hardware architectures for artificial neural networks are developed within the electronic platform, integrated photonics is emerging as a fast and efficient alternative. The way in which information is elaborated inside neural networks seems to be more favorable, in comparison to the boolean logic, to the development of photonic integrated processors [29]. The aim of photonics is to match the performances of electronics in the development of neuromorphic networks by exploiting its inherent suitability to parallel computing, its bandwidth and speed, and also its power efficiency (see Table 2.2).

| Chip | MAC rate | Energy per MAC (pJ) | Area per MAC (μm^2) |
|---|----------|------------------------|-------------------------------------|
| Photonic hybrid III-V/Si | 20 GHz | 1.3 | 205 |
| Sub- λ photonics (future trend) | 200 GHz | 0.0007 | 20 |
| HICANN | 22.4 MHz | 198.4 | 780 |
| TrueNorth | 2.5 kHz | 0.27 | 4.9 |
| Neurogrid | 40.1 kHz | 119 | 7.1 |
| SpiNNaker | 3.2 kHz | 6×10^5 | 217 |

Table 2.2: Comparative table on current and future trends in electronic and photonic micro-architectures for neuromorphic computing. MAC stands for *Multiply and ACcumulate* operation, a standard computational step. Taken from [10].

Nevertheless building a neural network within a photonic integrated chip is a demanding task. For this reason, the results achieved until now have been obtained by using a small number of integrated devices. This fact inevitably limits the maximum complexity of the neural networks built. However, many neuromorphic networks are based on the reservoir computing (RC) approach or the recurrent neural network (RNN) type or both. The first one is a learning method that allows to have little to no control on the majority of the network while employing all efforts on the training of a single output layer [30], [31]. Hence very fast and complex system can be exploited without having real control on the local effects that happen inside the *reservoir*. On the other hand, a recurrent neural network can be implemented with only one computational node [31], [32], as it exploits time to distribute the computation. In this type of network, the lack of physical complexity is compensated by the extension in time of the required task.

The idea of this work is to tackle the problem head on and develop a framework for feed-forward artificial neural network based on optical effects.

As shown in Section 1.2, the principal parts of an artificial neural network are its nodes, which in turn are built by two separate subcomponents: the weighted sum and the nonlinear activation function. In the next sections I will describe how the nonlinear response of a microring could be exploited in an all-optical node of a feedforward ANN.

2.4.1 Weighted sum of inputs

The difficulty in the weighted sum of inputs does not lie in the type of operation, i.e. sum and multiplication, but in the fact that each node has many inputs. Excluding the cases in which the weighted summation has been carried off by online or offline elaboration on standard computers, there are two important examples of all-optical weighted sum.

The first one [33] is based on a cascade of Mach-Zehnder Interferometers (MZI), which transforms all the outputs of a whole layer to the set of inputs of the next one. This happens by a sequence of constructive and destructive interferences that alter the starting coherent signal.

The second example [34] is given by a series of microring resonator, parametrically tuned to transmit a portion of light. In this work, different signals are multiplexed on many wavelengths and are weighted by consecutive rings built in such a way that they affects only a certain wavelength. Moreover, the weight is implemented by thermal finetuning of the resonator cavities. This example, however, exploit an optoelectronic nonlinear stage composed of two photodiodes and a light source nonlinearly dependent to the current produced by the photodiodes.

2.4.2 Nonlinear Activation Function

The development of novel optical mechanisms for the nonlinear activation function in ANNs has not progressed as much as the development of the weighted sum of the node inputs has. In fact, many proposed PICs by means of integrated optical structures realize the weighting part of the inputs only. The nonlinear activation function is then implemented either by electronic devices [34] or even by computer aided evaluation [33].

An interesting proposal is to employ a saturable absorber to obtain a nonlinear activation function [32]. Saturable absorbers are materials that have a reduced absorption of light for high optical intensities.

The idea of my work is to employ the optical bistability in a microring resonator as a mean to obtain a nonlinear activation function, that simulate the commonly used sigmoid one. Optical bistability, as seen in Subsection 2.3.4, is an optical effect that occurs when injecting light in a microring resonator with a lower frequency in respect to the resonance frequency.

In a quasi-static regime, optical bistability is mainly due to the therm-optic effect, which depends from the temperature. However, temperature depends in turn from the optical power circulating inside the cavity, which is obviously determined by the input intensity. This allows to obtain a total output transmission that depends nonlinearly on the input intensity.

2.4.3 Simulations

In order to better understand the physical mechanisms underneath the microring behavior, I used numerical methods to simulate the response of a microring resonator. Since the experiments are carried out in the quasi-static regime, the system can be described by a set of three coupled algebraic equations: one for the enhancement factor, one for the free carrier dynamics, and one for the thermal dynamics.

$$EF(\omega) = \frac{\gamma \Delta \gamma}{(1 - \tau^2 \gamma \Delta \gamma)^2 + 4\tau^2 \gamma \Delta \gamma \sin^2 \left((n_{eff} + \Delta n_{eff}) \frac{\omega}{c_0} \pi R \right)} \quad (2.39)$$

$$\Delta N = \frac{1}{\gamma_{FC}} \frac{\beta_{TPA}}{2\hbar\omega} I^2 \quad (2.40)$$

$$\Delta T = \frac{1}{\gamma_{TH}} \frac{1}{M_{ring} C_p} V \left(\alpha_{eff} + \beta_{TPA} I + \frac{d\alpha}{dN} \Delta N \right) I \quad (2.41)$$

where

$$I = EF I_{input} \quad (2.42)$$

$$\Delta \gamma = e^{-\left(\beta_{TPA} I + \frac{d\alpha}{dN} \Delta N \right) \pi R} \quad (2.43)$$

$$\Delta n_{eff} = n_2 I + \frac{dn}{dN} \Delta N + \frac{dn}{dT} \Delta T \quad (2.44)$$

This set of equations allows a simple but complete description of the physical quantities of interest in the system.

To decrease numerical errors, a reduced variable approach has been used. This means that every factor in the equations has been divided by the order of magnitude typical of the problem, to reduce or increase its numerical representation towards unity. For examples, distances have been reduced to μm and powers to mW and so on.

In addition, important values that are not explicitly computed, such as the transmission of the through and drop channels, can be extracted with just a simple multiplication. Moreover, adding another light source at a different wavelength (or frequency) is very simple. It is obtained by adding a second equation for the enhancement factor $EF(\omega_2)$ and by redefining the optical intensity circulating inside to $I = EF(\omega_1) I_{input}(\omega_1) + EF(\omega_2) I_{input}(\omega_2)$. This neglects interference effects between the two beams, but then again the whole evaluation is a first-order-approximation.

To obtain the correct values that verifies the set of equations, I employed an iterative algorithm. First of all I assume a certain set of initial conditions for EF , ΔN , and ΔT , which I will call $EF|_0$, $\Delta N|_0$, and $\Delta T|_0$ respectively. For example one could choose to start from a *cold* system by setting them to zero. Then I evaluate the values the same variable at the next step by parametrically replacing the variables with their newly discovered values.

$$\begin{aligned} 1) \quad & EF|_1 = EF(\omega, EF|_0, \Delta N|_0, \Delta T|_0) \\ 2) \quad & \Delta N|_1 = \Delta N(EF|_1, \Delta N|_0, \Delta T|_0) \\ 3) \quad & \Delta T|_1 = \Delta T(EF|_1, \Delta N|_1, \Delta T|_0) \end{aligned}$$

which is easily generalized by putting $|_0 \rightarrow |_n$ and $|_1 \rightarrow |_{n+1}$. These three steps must be repeated until they converge to a steady state value.

At low input intensities nonlinearities are negligible, thus the output has the shape of the *cold* resonance, as shown in Figure 2.12.

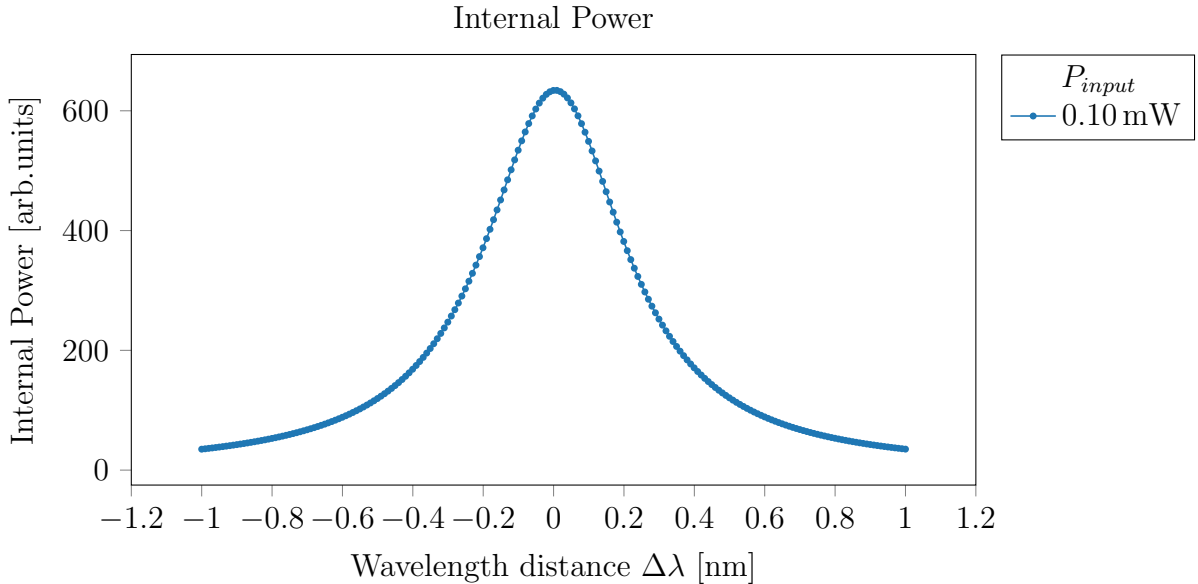


Figure 2.12: Shape of the resonance when probed with a low intensity signal. As expected is a lorentzian-type of curve, like in Figure 2.6.

At higher intensities the nonlinear effects become non negligible and therefore the number of iteration required increases. The algorithm evolution follows the same steps of the physical system: the system start off in a *cold* state and the gets progressively heated by the light that gets coupled inside the cavity.

However, the optical bistable region is also a region of instability for the algorithm, because there are two stable and infinite unstable states. As for the physical system, which selects the

state depending on the past condition of the cavity, the same happens for the algorithm. By choosing as initial conditions the output values of the the variables obtained by the evaluation of the previous set of parameters, proved to be a successful approach to the problem.

Still, this method is not enough at high intensities, when the algorithm could not reach a steady state value due to the high number of iterations required. This is due to the fact that in certain regions, the values of consequent iterations oscillate around the steady state without any tangible progress toward convergence. This drastically increases the number of iteration required. For this reason I modified the algorithm from the vanilla iteration above to a more complex one. In this revised algorithm the variables at each new step are evaluated with a mix of the last and second to last values instead of just the last one. This method contrasts the phenomenon of uncontrolled value oscillation.

The results of the algorithm, for input parameters given by a sequence of signals of increasing optical power at a precise distance from the resonance wavelength, map half of the hysteresis cycle. It is important in this case to set the initial conditions as the output values of the last evaluated state. Similarly, by setting the input parameters with a sequence of signals of decreasing optical power, the results map the other half of the bistability hysteresis cycle. The collection of the outcomes, obtained by repeating this evaluations for a set of different wavelengths on the red shoulder of the resonance, is shown in Figure 2.13.

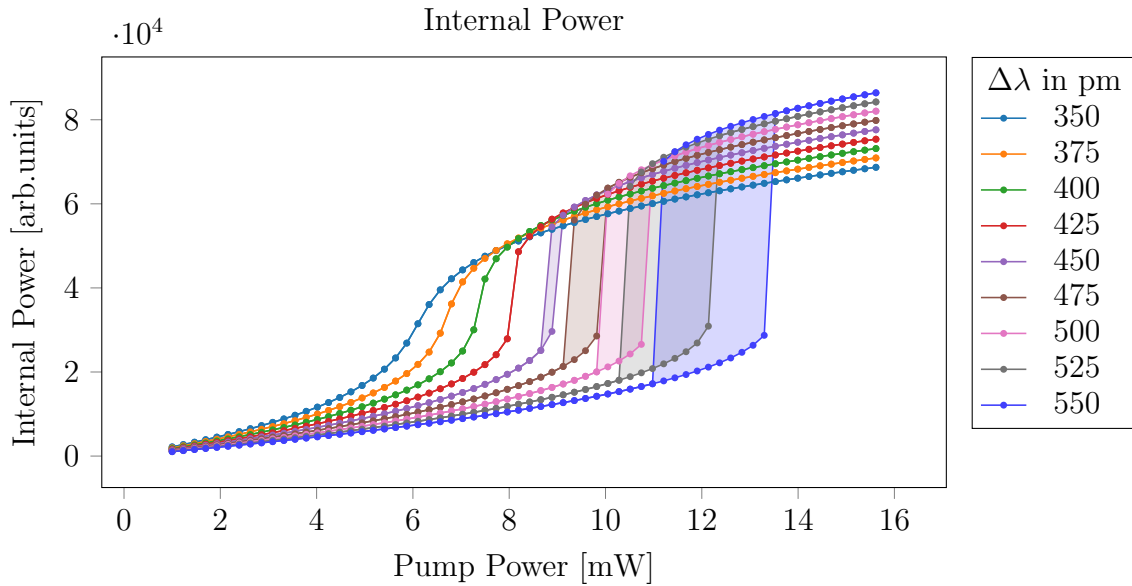


Figure 2.13: Hysteresis cycles described by the increase and decrease cycle of power, for input beams at different separations from the *cold* resonance wavelength, in pm. All cases have higher wavelength (lower frequency) in comparison to the resonance wavelength.

The simulations predict that, for wavelengths near the resonance, the hysteresis cycle will disappear in a single curve, similar to a sigmoid. Forward and backwards sweeps will coincide in this case. On the other hand, inputs at farther wavelength from the resonance will show an increasing area of bistability and the jumps at the edges of the bistability regions are more sharp for higher input powers.

Another interesting way to map the bistability effect is to set the initial conditions for a fixed input optical power at a shorter wavelength than the resonance wavelength. Then evaluate a certain number of sample wavelengths in a progressive sweep toward longer wavelengths until the whole shape is mapped. Also in this case it is important to set the initial conditions of each run as the output values of last evaluation. Similar results can be obtained by inverting

the sweep, thus showing another type of hysteresis cycle. Figure 2.14 shows an example of this behavior.

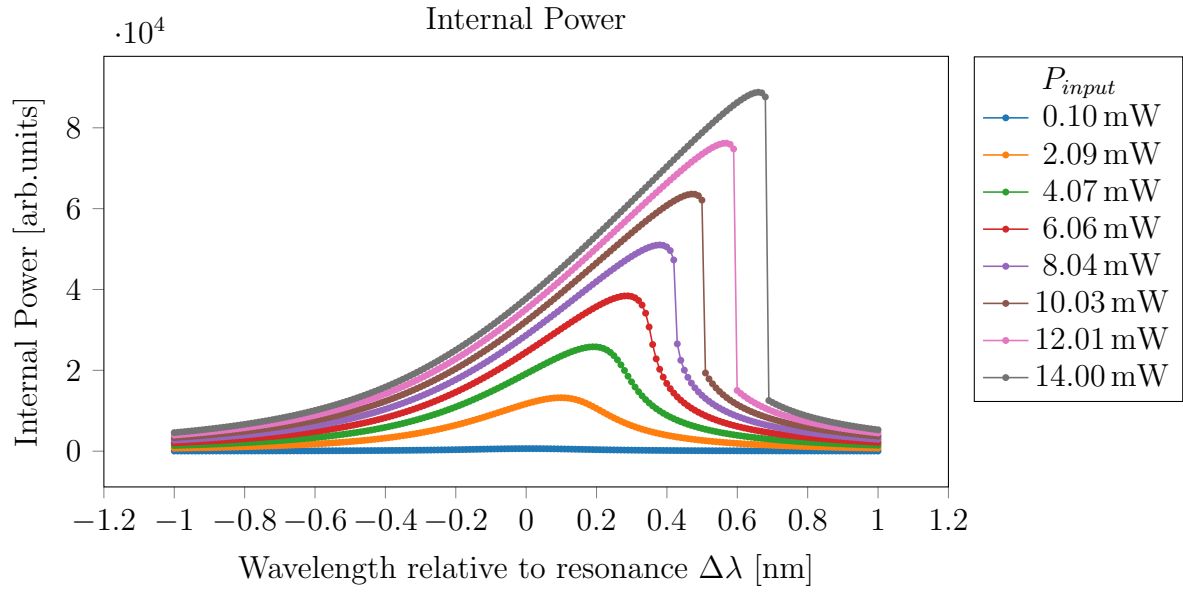


Figure 2.14: Behavior of wavelength sweeps for fixed input optical powers. The lower curve (blue), is the same portrayed in Figure 2.12.

Chapter 3

Samples, setup and experiments

All the experiments have been carried out on samples manufactured for the IRIS project [35]. This is due to the fact that in the time frame of this work there would have not been enough time to design and produce an ad hoc device. Moreover, as already stated, the aim of this thesis is to produce a proof of concept for an all-optical implementation of an activation function, rather than to construct a complete prototype. With the knowledge obtained during this work, future researches could design new structures by focusing on the correct parameters.

3.1 The samples

The IRIS project studied the design and the implementation of an integrated reconfigurable silicon photonics switch matrix, a routing device, as a replacement for electronic devices used in the telecommunication industry. The completed integrated photonic circuit consists of a matrix of waveguides crossing each other and linked by couples of racetrack resonators, thermally-controlled. At the ends of the waveguides other structures, interleavers and AWGs, allowed many signals at different wavelengths to be multiplexed/demultiplexed onto/from the same waveguide.

The complexity of such photonic circuit required outstanding precision in the design and the fabrication. Hence, for preliminary testing purposes, each and every structure of which the full device is composed, has been manufactured repeatedly with several small variations. For example, several microrings in the ADF configuration have been fabricated with different radius, or different ring-waveguide gap. The collection of all these testing structures on the same chip was produced in a few samples. All these test structures as well as a fully completed switch matrix were disposed on a single chip, accessible via grating couplers.

The first step of this work therefore has been to characterize qualitatively the response of some devices among the single structures, the short sequences of structures, and the full switch matrix itself. After many trials of different devices, my final choice was to study a system of intermediate complexity. In fact, since the work in this thesis is like the first step in a long journey, with this choice I tried to obtain a compromise between simplicity in immediate future (current work) and adaptability in the long term. For example, the current structure allowed me to study the nonlinear activation function, but could be reused in the future to study the weighted sum.

The structure selected is the following: a simple waveguide, coupled to eight drop channels by a single or a couple of ring resonators each, nicknamed *mini-matrix*. In this family of devices, there were those built with single microrings, double microrings, single racetracks, or double racetracks. The final choice was to study the *mini-matrix* in which the coupling mechanism was provided by single ring resonators, because of its simpler transfer function in respect to double microrings or double racetracks. Figure 3.1 shows a magnified photograph of the device

chose, while Figure 3.2 shows a simplified (not in scale) scheme of the principal sub-structures of the *mini-matrix*.

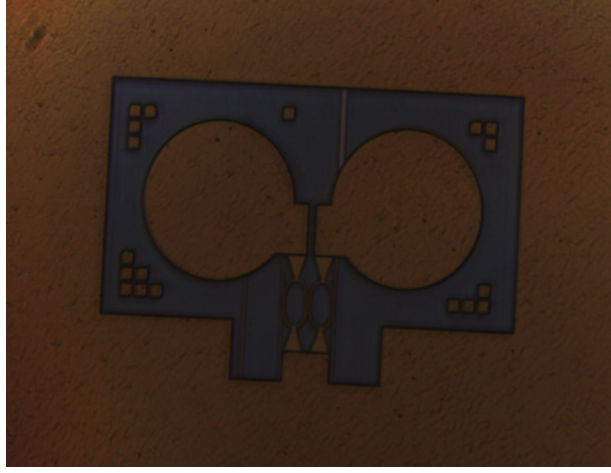


Figure 3.1: Magnified photograph of the *mini-matrix* device chosen. On the bottom, one input and nine output grating couplers are visible.

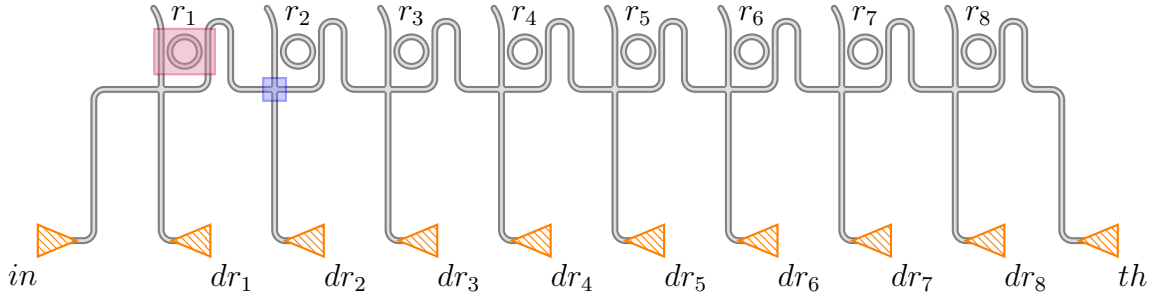


Figure 3.2: Simplified scheme of the *mini-matrix* integrated photonic circuit, structures are not in scale. Triangles (orange) are the grating couplers (in , dr_{1-8} , th), with the orientation respected by the symbol orientation. Waveguides and rings (r_{1-8}) are shown as thick grey lines. The bigger (purple) highlighted area is a coupling region, the smaller (blue) area is a crossing between straight waveguides. Bendings, crossings, and grating coupler are nontrivial structures which have their own typical response to wavelength and power.

As an additional feature, each one of the microring resonators in the structure has been manufactured with thermo-electric heaters. Their purpose [35] is to heat the rings and effectively shift the resonance frequency, which otherwise would be defined strictly by the geometry of the structure. Figure 3.3 shows the scheme of the microring resonator geometry, without any non-optical structure (e.g. heaters, metallic contacts).

3.1.1 Initial characterization

To obtain an initial characterization of the sample, I arranged an experimental setup to measure its fundamental attributes. Among them there are the position of the resonances, the free spectral range FSR , and the full width half maximum $FWHM$ of the resonance transmission function. These features can all be obtained through a study of the transmitted intensity in the through and drop channels, shown in Figure 3.2. A scheme of the experimental setup used in showed in Figure 3.4 below.

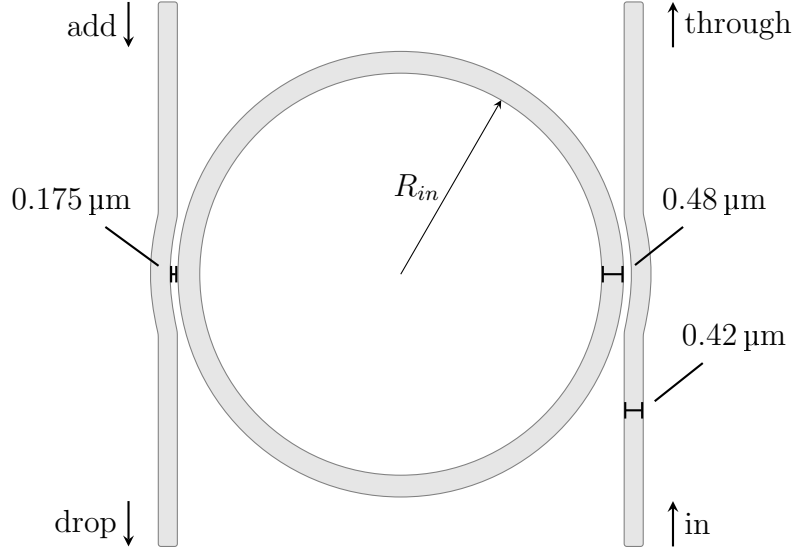


Figure 3.3: Microring optical cavity region, structures are in scale. The ring has an internal radius of $R_{in} = 4.43 \mu\text{m}$ and its width is of $0.48 \mu\text{m}$. The waveguides side coupled to the ring have a width of $0.42 \mu\text{m}$ and distance from the ring of $0.175 \mu\text{m}$.

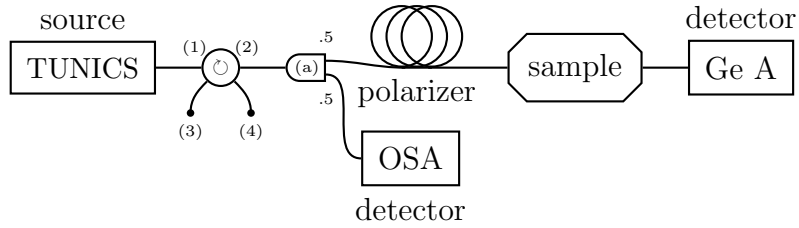


Figure 3.4: Scheme of the setup used to obtain an initial characterization of the sample. The source is a TUNICS which produces a laser beam of up to 8 mW in the range of wavelength required (1500 nm to 1580 nm). The second element is an optical circulator and the third is a fiber coupler (50%:50%). Within the coupler the signal is split. One arm goes to an Optical Spectrum Analyzer (OSA). The other arm takes the signal to a polarizer which is then injected into the sample and finally extracted to be read by a Germanium-based photodetector.

The laser source used in this measures is a Yamatsu TUNICS T-100S tunable infrared laser. It produces a linearly polarized continuous wave laser beam of optical power up to 8 mW in the wavelength range 1500 nm to 1580 nm, with a minimum wavelength step of 1 pm. The generated light is injected into an optical circulator to protect the laser cavity from back-reflections. A circulator is a device that works similarly to a roundabout: input signals from the first port are directed only toward the second port. Similarly, signals injected in the second port are guided in the third port only and so on. The circulator used in the setup has four ports. Afterwards the beam is divided into two equal parts by means of a fiber coupler: one is analyzed by an optical spectrum analyzer (OSA) and the other is brought to the sample.

The presence of an OSA after the source is due to the fact that the self-referencing mechanism of the laser was not reliable. In fact, the actual wavelength emitted from it deviated rather sensibly from the supposed one. In order to correct this problem, I sampled the supposed-actual wavelength relationship with the OSA, which allowed me to implement an online correction by exploiting the relative inverse function. In doing so, I assumed the OSA as a reference with no error.

All structures built on the test chip are accessible via grating couplers. Both the couplers and the photonic integrated circuits of IRIS are designed to support modes in the polarization TE only. Grating couplers are planar periodic structures engineered to couple light from free space into integrated waveguides and vice versa. Due to geometrical constraint, they are built to work in a specific range of wavelengths and at a certain angle. This means that light at wavelength in the predefined range, impinging on the grating coupler with the correct angle, is coupled inside the waveguide on the PIC. Similarly, light coming from a waveguide to a grating coupler, is radiated as plane wave from the grating coupler with the same mentioned angle.

The sample is therefore adjusted on a 2-DOF linear stage in between two 3-DOF linear stages that holds the input and output coupling fibers. Figure 3.5 shows the respective position of input and output fibers in respect to the grating couplers.

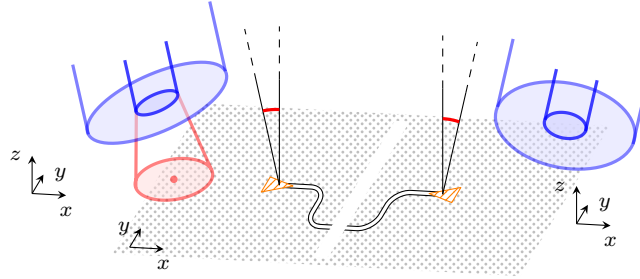


Figure 3.5: Alignment phase of the input and output fibers over the corresponding grating couplers. The optical fibers are aligned at an angle of 14° over the grating couplers in such a way to inject and collect as much light as possible. The sample was placed in a specific slot of a copper sample holder, which was secured onto a 2-DOF manual stage. The two fiber holders were placed on a 3-DOF manual stage each, to obtain best alignment. The angle of the fiber holder tip was fixed during the assembly at 14° from the surface normal.

Once secured the input and output optical fibers in place on the linear stages, the alignment phase begins. First the source is turned on at a wavelength that transmit on the correct channel, for example the resonance wavelength transmit in the drop channels but not in the through channel and vice versa. Then the optical fibers are carefully moved in the respective positions that maximize the coupled signal. This procedure needs meticulous practice and method to avoid errors due to noise and imprecise movements of the linear stages. Moreover, sometimes the procedure must be repeated even if neither the sample nor the fibers have been moved, because of mechanical relaxation processes of the inner gears.

To obtain the best results, I also designed two new modular fiber holders with fixed angle, that could be used more easily than the older ones with adjustable angle. The main body has been manufactured in aluminum, except for the actual part that sustains the fiber, which was produced in iron. The metallic tip of the holder, appropriately grooved to house the optical fiber, can hold still the fiber with the help of little magnets. This techniques aims to reduce as much as possible the vibration of the fibers ends which causes fluctuations in the amount of light coupled to the gratings.

Since the PICs developed for IRIS support TE modes only, after the positions of the optical fibers have been optimized, the coupled signal is maximized by the use of a polarizer. The polarizer, placed between the fiber coupler and the sample, is a device composed by a long optical fiber. Such fiber is coiled in three separate loops which have the effect of a half-wavelength plate, one quarter-wave plate, and another half-wave plate respectively. Each coil can be manipulated, in a similar manner to the bulky quater-/half-wave plates, to change the output (linear) polarization of the light. The position of the polarization stage before of after the OSA junction is not relevant as the OSA is polarization independent.

In order to reduce further the impact of noise on measures, I also boxed the three linear stages with stiff walls. This allowed to decrease the random fluctuations, due to movement of the fiber tips in the air, of at least one order of magnitude.

For the initial characterization of the structure, I studied the response of each output at input signals with low optical power and in a certain range of wavelengths (frequencies). With this study, I identified the position of the resonances and their shape. As shown in Figure 3.6, the through channel *th* follows the shape of the grating coupler response, which is centered around 1550 nm and slowly drops with the growing relative distance from that wavelength. Moreover, one can observe that the first drop channel *dr*₁ has the expected shape (lorentzian), with a free spectral range of $FSR = (19.15 \pm 0.10)$ nm. On the other hand, all the other drop channels show a transmission that is perturbed by the light collected in the first channel.

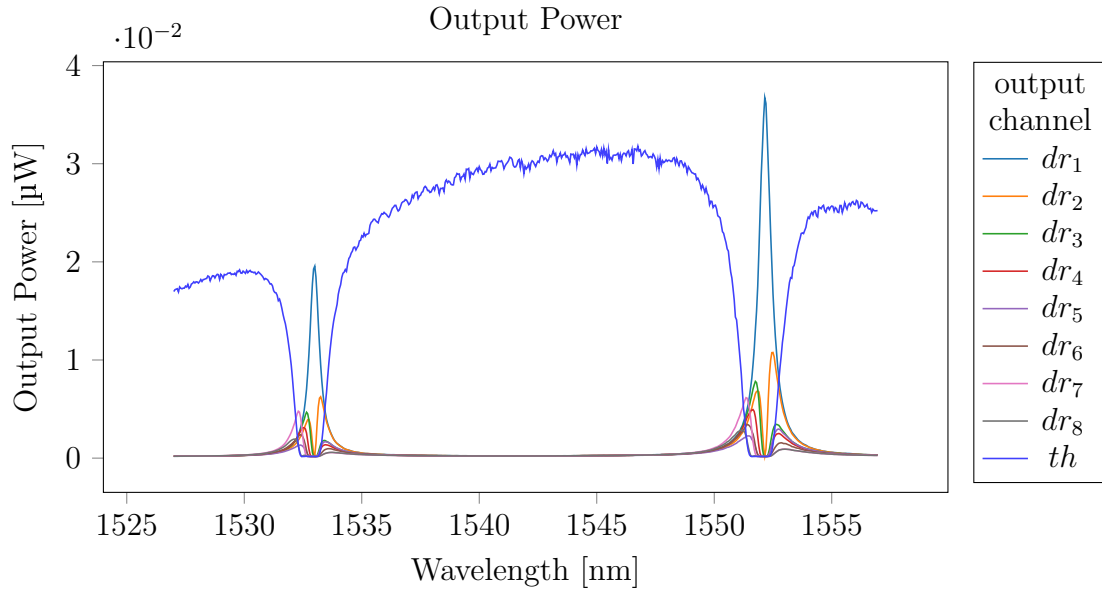


Figure 3.6: Transmission spectra of the drop channels (*dr*₁ to *dr*₈) and through channel *th*. The *dr*₁ channel shows the expected shape, whereas the other drop channels are clearly disturbed by the first one. The through channel shows a shape similar to the expected one, but it is actually the results of all the drop channels.

Since the the first channel is the only one with an unperturbed transmission, I focused my attention on its response only. Specifically, I studied the resonance near 1550 nm because it

was the one with the highest transmitted signal and hence provided a better SNR. Figure 3.7 shows such resonance and highlights its width to $FWHM = (0.6 \pm 0.1) \text{ nm}$?. The estimated quality factor is $Q = 2600 \pm 400$??.

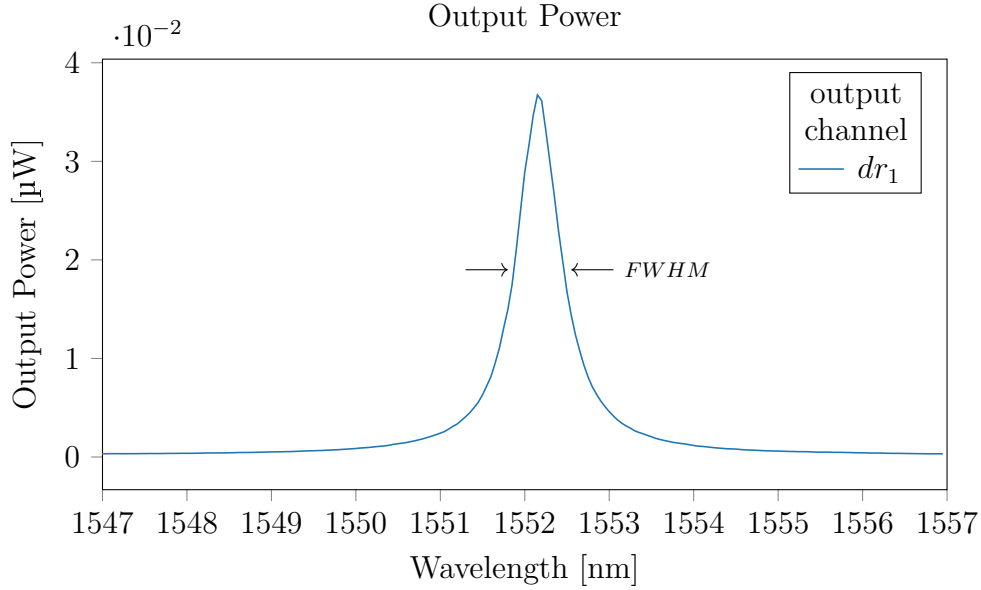


Figure 3.7: Resonance near 1552 nm, transmission to the drop port dr_1 . This spectrum is the only one unperturbed by the other transmission spectra. The FWHM and the resonance wavelength are clearly visible in the figure.

3.2 Characterization of the Activation Function

To characterize the thermal bistability of the microring resonator the setup used for the initial measures was not enough. In order to induce the thermal bistability effect in the microring I amplified the signal of the TUNICS with an Erbium-Ytterbiym-Doped Fiber Amplifier (EYDFA). Even more so with addition of the optical amplifier, the role of the circulator placed between the sources and the rest of the devices is of fundamental importance. Back-reflected signals that enter optical amplifier in the wrong direction can cause serious damage to the equipment.

In addition to the amplifying stage, a remotely controlled *variable optical attenuator* (VOA) was added between the polarizer and the sample, in order to characterize with accuracy the response of the microring resonator to signals of fixed wavelength but different optical power. The VOA employed is controlled by a voltage signals in the range 0 V to 5 V. It provides full transparency for 0 V and full attenuation for 5 V and, in between, the attenuator behaves similarly to a sigmoid function. This curve has been identified with its closest analytical polynomial, to obtain an inverse formula that links transparency values in the range $[0, 1]$ to the respective correct voltage value.

Theoretically, this setup is sufficient to measure the features of the bistability effect. However, due to instabilities of the source and amplification stages, both in the optical power and in the wavelength of the signal, that is not the case. Hence, an additional infrared photodetector was placed before the VOA, completing the setup as shown in Figure 3.8.

The second infrared detector measures a small part (10%) of the signal, which is collected from the main path via a fiber coupler (90%:10%). Hence, in this configuration, the OSA provides control over the wavelength of the source, while the photodetector provides control over the power emitted. Unfortunately, the measures obtained by means of the OSA, due to intrinsic limitations of the instrument and to the high complexity of the measure itself, have

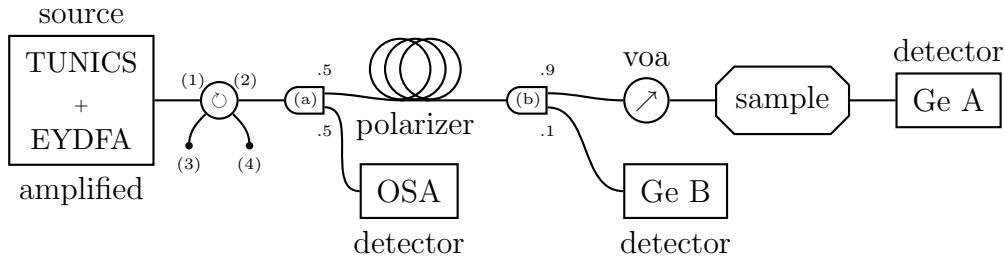


Figure 3.8: Scheme of the setup used to obtain characterization of the thermal bistability in the microring resonator. The source (TUNICS) is amplified by an EYDFA, which can reach optical power up to several hundreds of mW. The amplified source is followed by the circulator and by the fiber coupler (50%:50%), that splits the signal to the OSA and to the polarizer. After the polarizer, a second fiber coupler (90%:10%) direct a small part of the signal to a second Germanium-based photodetector. The signal in the other arm passes through a Variable Optical Attenuator (VOA), then it is injected into the sample, and finally extracted to be read by a Germanium-based photodetector.

a much lower sampling rate in comparison to the measures given by the photodetectors. For this reason, the OSA has been employed as a before-and-after check on the light emitted by the source stages.

On the other hand, the second infrared detector was inserted in the measuring loops such that it collected data for each sampled point. Therefore, the data collected is composed by the optical power measured before the VOA, by the transparency of the VOA, and by the optical power measured at the output. This three-point measurement allowed more robustness against power fluctuations.

3.2.1 Bistability wavelength dependence

The first feature studied is the dependence on wavelength of the overall shape of the bistability hysteresis loop. As seen in Subsection 2.4.3, the form of the bistability changes with the distance of the wavelength of light in respect to the wavelength of the resonance. This behavior is also observed in the transmission spectra experimentally measured, as shown in Figure 3.9 below.

As expected, the region of bistability disappears for wavelength within a certain distance from the wavelength resonance. Moreover, by increasing the distance between the pump and the resonance wavelengths, the bistability region becomes larger. The range of wavelengths with which the sample has been probed is upper limited due to the growing pump power required to activate the bistability.

HOW DOES THIS COMPARE TO THE SIMULATIONS?

Bistability region edges

In order to describe with more precision the abrupt jumps on the edges of the bistability region, I also set up specific measurement loops. These loops repeatedly initialized the system with the VOA at full absorption and then characterized the jump by sampling from few points below to few points above the bistability step. Similarly, the other *inverse* bistability step was characterized by analogous loops in which the system was initialized with the VOA at full transparency instead.

Eventually the data collected included twenty loops for each wavelength selected, which are five almost equally spaced in a wavelength range from 1552.2 nm to 1552.3 nm. Each of this loop has been analyzed to find the abrupt jumps from a state to the other. A simple study

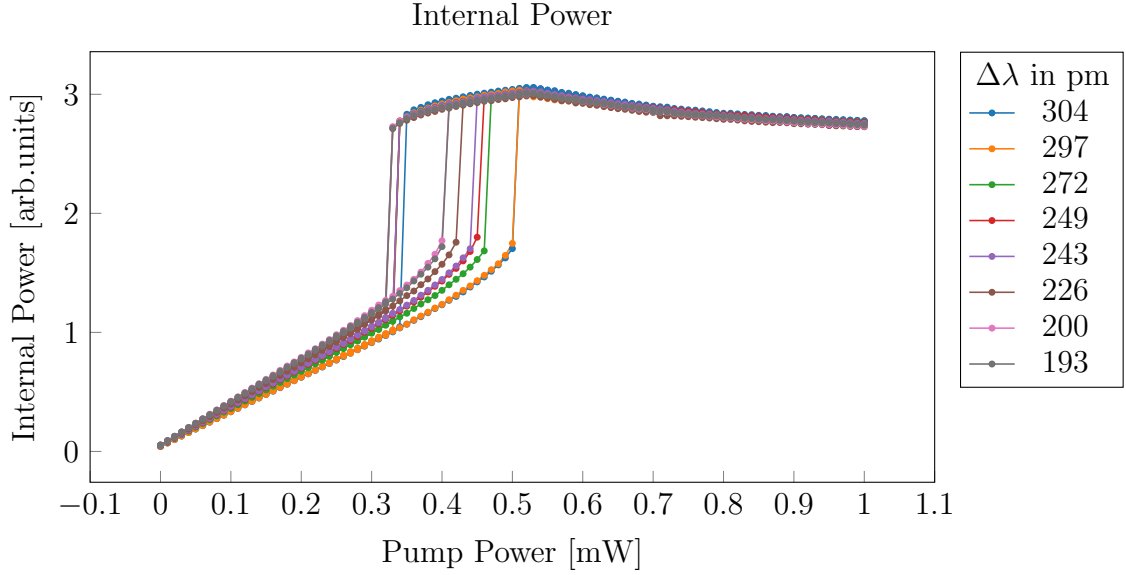


Figure 3.9: Many bistability loops at different wavelengths. The loops that are closer to the microring resonance have smaller bistability regions or they have not one at all. Loops that are farther from the resonance have larger bistability regions.

on the discrete derivative was employed to achieve that. The same procedure has been applied both to the rising loops and to the descending loops. The results are five data points for the first kind of loops and just as much for the descending loops, as shown in Figure 3.10.

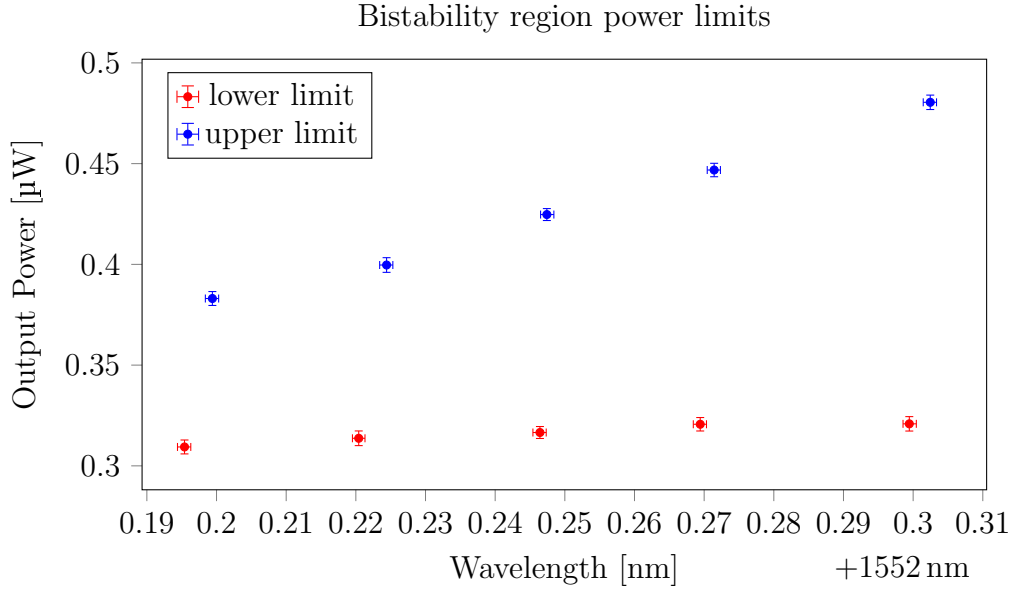


Figure 3.10: Wavelength dependence of the bistability region edges. Upper limits are shown as blue dots, while lower limits are shown as red dots. The wavelength uncertainty is assumed to be 1 pm for all the points and it is an estimate given by checks in between consecutive measures obtained with the OSA. The power uncertainty is given by the statistic of the data collected with the loop in power.

The error on each point has been evaluated as follows. The uncertainty on the wavelength position is an estimate, given by checks on the spectrum of the source, obtained with the OSA before and after each measure cycle. The uncertainty of the power is calculated on the statistic

of all the loops measured at the same wavelength. Hence it is defined as the RMS error of twenty data points for each wavelength.

It is interesting to observe that the experimental data, much like the simulations, show a steeper dependence on wavelength for the upper limits than for the lower limits. Nevertheless, both quantities seem to increase with wavelength more distant from the resonance. Moreover, the position of the edges of the bistability region seem to be precisely defined by the parameters of the system.

3.3 Test of a Trained ANN

The first step that I made in order to test the nonlinear response of a microring resonator as a neural network activation function is to exploit the fitted bistability curve of Equation 3.1 and implement it as activation function of the model defined in Subsection 1.5.3.

3.3.1 Optical bistability as nonlinear activation function

Having obtained a description of the optical bistability of the response of a microring resonator in a wide range of wavelengths, I implemented the shape of such response in a simulated artificial neural network. Hence, I chose one set of data from the group, such that it was neither the most distant nor the closest to the resonance. This was made to avoid unexpected “border effects”. Specifically, the data belongs to the increasing half of the bistability loop for input light at 1552.300 nm ??.

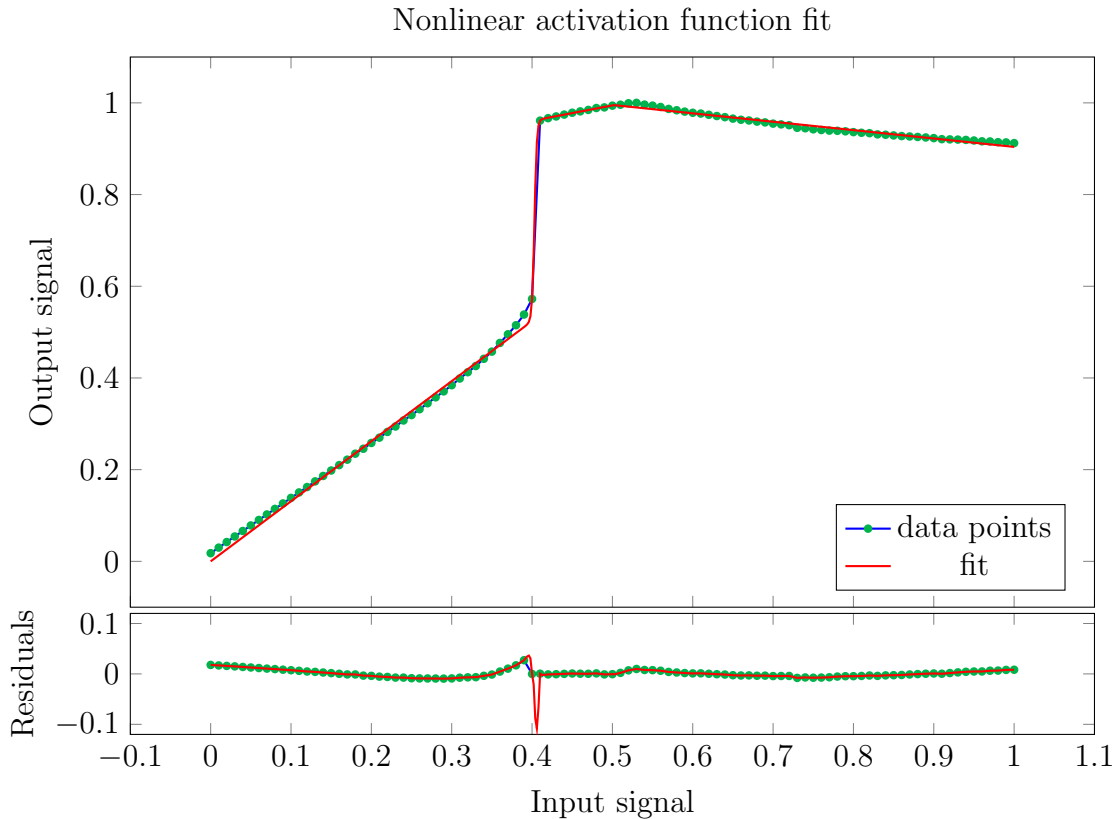


Figure 3.11: Curve fitting and residuals on a set of data. The nonlinear curve is the increasing half of a bistability loop. The fit is quite close to the original values, except near the jump.

The curve employed to fit the data is a combination of function that are already implemented

in PyTorch library. This allows a simple implementation in the simulations. Specifically the function is composed by *Logistic* and *ReLU* function

$$f_{fit} := b f_{Logistic}[a(x - x_0)] + c f_{ReLU}[x] + d f_{ReLU}[x - x_0] + e f_{ReLU}[x - x_1], \quad (3.1)$$

where the parameters a , b , c , d , e , x_0 , and x_1 are fixed by the fit.

As shown in Figure 3.11, the curve fit on the chosen dataset is very close to the original data points. This is true all over the range of powers, except near the bistability edge, where the maximum difference occurs.

3.3.2 Optical bistability vs ReLU and Logistic

HO PROVATO DIVERSE GEOMETRIE e DIVERSE LOSS FUNCTIONS

COME ADATTARE I PESI VIRTUALI A QUELLI FISICI? rappresentazione a bassa precisione?

Conclusion

Summary

This work was focused on using an optical microring resonator as nonlinear node of a feedforward artificial neural network. The problem has been tackled simultaneously by two directions: the experimental measurement of the nonlinear response of the node and its simulation by means of software libraries.

The first part of the thesis aimed to introduce the fundamental concepts of artificial neural network and machine learning. It was followed by the arrangement of a simulated neural network on the PyTorch software library.

The central part of the thesis explained the physical effects related to the working principles of an optical microring resonator in the *Add-Drop Filter* configuration. These effects initially have been studied in their analytical linear approximation. Subsequently, nonlinear perturbations have been introduced to the resonator response. The physical effect produced have been analyzed numerically.

In the last part, my work has been to assemble an experimental setup and a related measurement methodology. This setup has been used to gather experimental data on the actual response of an optical microring resonator.

Afterwards, the gathered data proved to be useful in the implementation, inside the simulated artificial neural networks, a nonlinear activation function resembling the response of the resonator.

Accomplishments

During the period of time of this work I assembled the experimental setup to study the integrated photonic device. The experimental measures have been carried out with a continuous enhancement of the setup.

The properties and the physical mechanisms that regulate operation of the resonator have been characterized. To obtain a more profound knowledge of the physical phenomena, I successfully carried out numerical simulations.

I implemented a small neural network in PyTorch, which is a software library used by the machine learning community. The code was initially used to solve a benchmark problem, with standard artificial neural network parameters and functions. Finally I implemented also a new activation function that mimics the response of a microring resonator in Add-Drop Filter configuration. This allowed me to confront the operation of the standard function with the one based on the optical bistability.

Improvements

The setup should be enhanced by working on its bottlenecks, which are, in particular, the light source and the photodetection system. The light source should be stabilized as much as possible, both in power and in wavelength. This is worth because the microring resonators are quite sensitive to the parameters of the input signals.

On the other hand, the system of the photodetectors could be improved in the response time as well. In fact, due to both hardware and software limitations, a full measure can take a long

time, depending on the number of sampling points. The photodetectors should be rearranged in a way such that their control could be simplified. Moreover, the control software has been developed to be adaptive rather than fast in its operation. Working on both the software and the hardware of the detectors should improve the single measurement speed. Hence, the time spent on the full measure will benefit too.

A better experimental setup would allow to acquire more data in less time and therefore to obtain a superior statistics. In turn this data, collected with a robust method, will consent also to complete a quantitative analysis. From this new work elaboration speed, energy efficiency, and requirements for node cascability could be estimated. Eventually this will help the design of a class of new ad hoc devices, whose characteristics will be defined suit neural network nodes operation.

Future perspective

As much important as the accomplishments, the futures studies which can start from this work or make use of part of it are many and interesting.

First of all, the natural continuation on this work on feedforward neural networks can start with the improvements suggested above. Improve the experimental setup, explore new zones in the parameters space and realize a quantitative analysis. Hopefully, this will lead to the definition of an all-optical framework for feedforward neural network development and operation.

Moreover, starting from the same framework with or without some modifications, an interesting development will be to research on the methods employed by reservoir computing. All-optical reservoir computing could put together the efficiency of the algorithm to the inherent complexity of structures based on multiple coupled optical cavities.

Furthermore, the development of a time-dependent theory would allow the analysis of physical effects in different regimes other than the quasi-static one. This will consent to investigate new phenomena and test their properties against the requirements for the neural network node operation. By exploiting new optical effects, we will be able to examine other implementations, such as spiking neurons. In this type of neurons, the intensity of the signals is as much important as their rate.

In common to all these projects, there must be a simultaneous development of the software simulation, based on standard libraries. This allows initial performance comparison between the software functions and the proposed physical effects.

Bibliography

- [1] M. D. Godfrey and D. F. Hendry, “The computer as von neumann planned it”, *IEEE Annals of the History of Computing*, vol. 15, no. 1, pp. 11–21, 1993.
- [2] F. Rosenblatt, “The perceptron: A probabilistic model for information storage and organization in the brain.”, *Psychological review*, vol. 65, no. 6, p. 386, 1958.
- [3] J. E. Stone, D. Gohara, and G. Shi, “Opencl: A parallel programming standard for heterogeneous computing systems”, *Computing in science & engineering*, vol. 12, no. 3, pp. 66–73, 2010.
- [4] F. Bastien, P. Lamblin, R. Pascanu, J. Bergstra, I. J. Goodfellow, A. Bergeron, N. Bouchard, D. Warde-Farley, and Y. Bengio, “Theano: New features and speed improvements”, *CoRR*, vol. abs/1211.5590, 2012. arXiv: [1211.5590](https://arxiv.org/abs/1211.5590). [Online]. Available: <http://arxiv.org/abs/1211.5590>.
- [5] R. A. Nawrocki, R. M. Voyles, and S. E. Shaheen, “A mini review of neuromorphic architectures and implementations”, *IEEE Transactions on Electron Devices*, vol. 63, no. 10, pp. 3819–3829, 2016.
- [6] *Humanbrainproject.eu*. [Online]. Available: <https://www.humanbrainproject.eu/en/silicon-brains/>.
- [7] H. Markram, “The human brain project”, *Scientific American*, vol. 306, no. 6, pp. 50–55, 2012, ISSN: 00368733, 19467087. [Online]. Available: <http://www.jstor.org/stable/26014516>.
- [8] M. Foedisch and A. Takeuchi, “Adaptive real-time road detection using neural networks”, in *Proceedings. The 7th International IEEE Conference on Intelligent Transportation Systems (IEEE Cat. No.04TH8749)*, Oct. 2004, pp. 167–172. DOI: [10.1109/ITSC.2004.1398891](https://doi.org/10.1109/ITSC.2004.1398891).
- [9] S. Soman, M. Suri, *et al.*, “Recent trends in neuromorphic engineering”, *Big Data Analytics*, vol. 1, no. 1, p. 15, 2016.
- [10] T. F. de Lima, B. J. Shastri, A. N. Tait, M. A. Nahmias, and P. R. Prucnal, “Progress in neuromorphic photonics”, *Nanophotonics*, vol. 6, no. 3, pp. 577–599, 2017.
- [11] W. S. McCulloch and W. Pitts, “A logical calculus of the ideas immanent in nervous activity”, *The bulletin of mathematical biophysics*, vol. 5, no. 4, pp. 115–133, 1943.
- [12] D. O. Hebb *et al.*, *The organization of behavior: A neuropsychological theory*, 1949.
- [13] B. Farley and W. Clark, “Simulation of self-organizing systems by digital computer”, *Transactions of the IRE Professional Group on Information Theory*, vol. 4, no. 4, pp. 76–84, 1954.
- [14] N. Rochester, J. Holland, L. Haibt, and W. Duda, “Tests on a cell assembly theory of the action of the brain, using a large digital computer”, *IRE Transactions on information Theory*, vol. 2, no. 3, pp. 80–93, 1956.

- [15] F. Rosenblatt, “The perceptron a perceiving and recognizing automaton”, *tech. rep., Technical Report 85-460-1*, 1957.
- [16] M. L. Minski and S. A. Papert, “Perceptrons: An introduction to computational geometry”, *MA: MIT Press, Cambridge*, 1969.
- [17] C. Clabaugh, D. Myszewski, and J. Pang, *Neural networks - history*, 2000. [Online]. Available: <https://cs.stanford.edu/people/eroberts/courses/soco/projects/neural-networks/History/index.html>.
- [18] R. O. Duda, P. E. Hart, and D. G. Stork, *Pattern classification*. John Wiley & Sons, 2012.
- [19] *Pytorch.org*. [Online]. Available: <http://pytorch.org/about/>.
- [20] *Uc irvine machine learning repository*. [Online]. Available: <http://archive.ics.uci.edu/ml/index.php>.
- [21] *Corning optical cable*. [Online]. Available: <https://www.corning.com/optical-cables-by-corning/worldwide/en/products/thunderbolt-optical-cables.html>.
- [22] G. T. Reed, *Silicon photonics: The state of the art*. John Wiley & Sons, 2008.
- [23] B. E. Saleh, M. C. Teich, and B. E. Saleh, *Fundamentals of photonics*. Wiley New York, 1991, vol. 22.
- [24] G. Agrawal, *Applications of nonlinear fiber optics*. Academic press, 2001.
- [25] S. Chen, L. Zhang, Y. Fei, and T. Cao, “Bistability and self-pulsation phenomena in silicon microring resonators based on nonlinear optical effects”, *Optics Express*, vol. 20, no. 7, pp. 7454–7468, 2012.
- [26] T. S. Moss, G. J. Burrell, and B. Ellis, *Semiconductor opto-electronics*. Butterworth-Heinemann, 2013.
- [27] M. M. Mancinelli, “Linear and non linear coupling effects in sequence of microresonators”, PhD thesis, University of Trento, 2013.
- [28] G. Priem, P. Dumon, W. Bogaerts, D. Van Thourhout, G. Morthier, and R. Baets, “Optical bistability and pulsating behaviour in silicon-on-insulator ring resonator structures.”, *Optics express*, vol. 13, no. 23, pp. 9623–9628, 2005.
- [29] B. J. Shastri, T. F. de Lima, A. Tait, M. A. Nahmias, and P. R. Prucnal, “Emergence of neuromorphic photonics”, in *Photonics in Switching*, Optical Society of America, 2017, PTu3C–4.
- [30] G. Van der Sande, D. Brunner, and M. C. Soriano, “Advances in photonic reservoir computing”, *Nanophotonics*, vol. 6, no. 3, pp. 561–576, 2017.
- [31] N. D. Haynes, M. C. Soriano, D. P. Rosin, I. Fischer, and D. J. Gauthier, “Reservoir computing with a single time-delay autonomous boolean node”, *Physical Review E*, vol. 91, no. 2, p. 020 801, 2015.
- [32] A. Dejonckheere, F. Duport, A. Smerieri, L. Fang, J.-L. Oudar, M. Haelterman, and S. Massar, “All-optical reservoir computer based on saturation of absorption”, *Optics express*, vol. 22, no. 9, pp. 10 868–10 881, 2014.
- [33] Y. Shen, N. C. Harris, S. Skirlo, M. Prabhu, T. Baehr-Jones, M. Hochberg, X. Sun, S. Zhao, H. Larochelle, D. Englund, *et al.*, “Deep learning with coherent nanophotonic circuits”, *Nature Photonics*, vol. 11, no. 7, p. 441, 2017.
- [34] A. N. Tait, T. F. Lima, E. Zhou, A. X. Wu, M. A. Nahmias, B. J. Shastri, and P. R. Prucnal, “Neuromorphic photonic networks using silicon photonic weight banks”, *Scientific Reports*, vol. 7, no. 1, p. 7430, 2017.

- [35] F. Testa, C. J. Oton, C. Kopp, J.-M. Lee, R. Ortuno, R. Enne, S. Tondini, G. Chiaretti, A. Bianchi, P. Pintus, *et al.*, “Design and implementation of an integrated reconfigurable silicon photonics switch matrix in iris project”, *IEEE Journal of Selected Topics in Quantum Electronics*, vol. 22, no. 6, pp. 155–168, 2016.

Acknowledgements